

results indicated that reduced VEGF levels in NP-C PNs caused a defect of autophagic degradation, but not induction.

Our findings that depletion of VEGF affects autophagic degradation prompted us to more closely examine how VEGF might influence in defective autophagic degradation. We first examined the transcription factor EB (TFEB), which coordinates lysosomal formation²⁴. VEGF depletion in WT PNs did not affect the levels of TFEB and Lamp1, indicating that VEGF did not impair lysosome biogenesis (Fig. 6e). Next, we assessed alteration in lysosomal pH using the acidotropic dye LysoTracker red. H₂O₂- and NH₄Cl-treated cells were used as positive and negative controls, respectively. VEGF siRNA-treated PNs exhibited a similar fluorescence to control siRNA-treated PNs, indicating that VEGF did not affect lysosomal acidification (Fig. 6f).

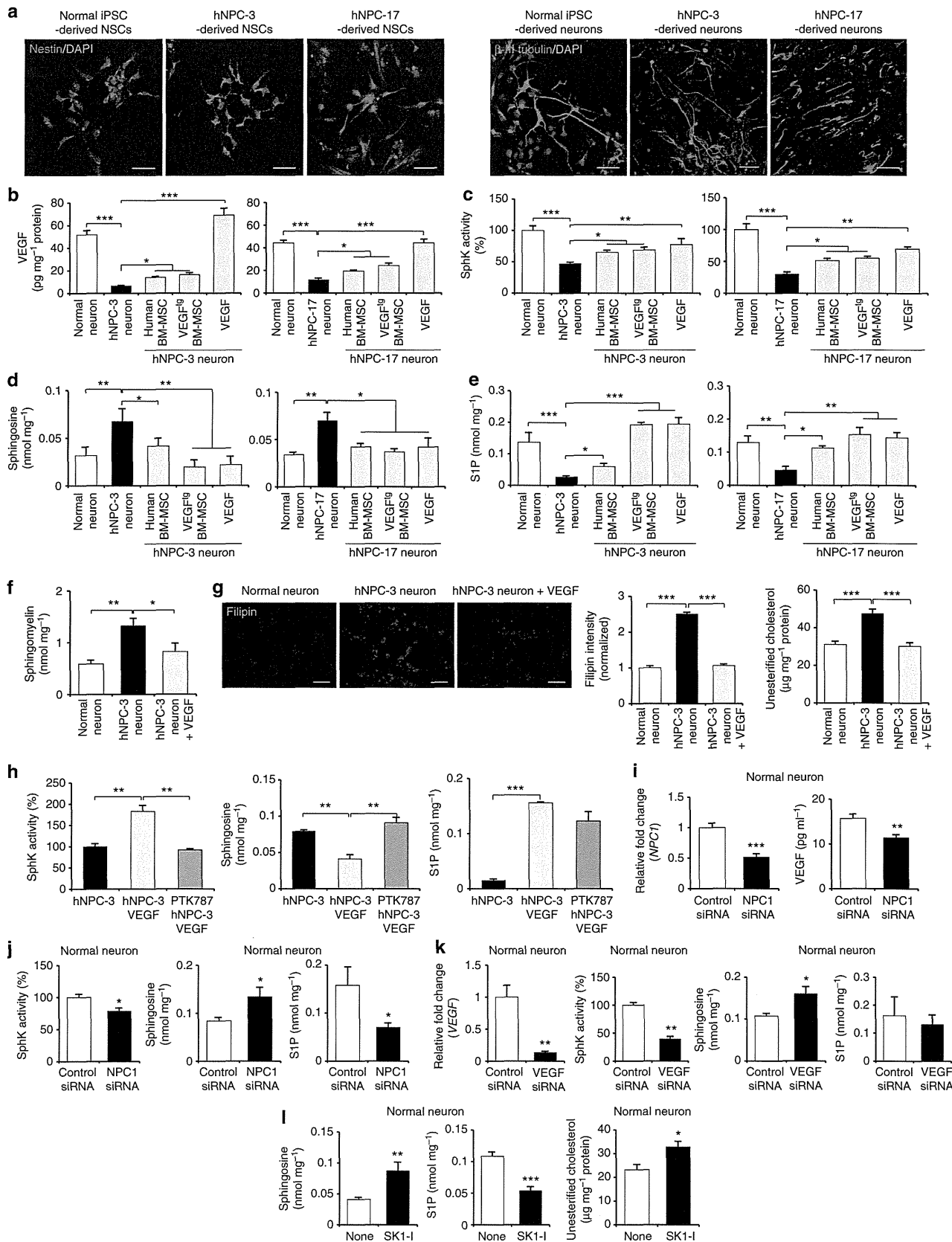
Following the initiation of the phagophores, autophagosomes undergo a stepwise maturation process from early to late autophagosomes, which ultimately fuse with lysosomes to form autolysosomes. To study the effect of VEGF depletion on the maturation of autophagosomes, we used mCherry-EGFP-LC3 reporter²⁵. Before fusion with lysosomes, the LC3-II-positive autophagosomes are shown by both GFP and mCherry signals as yellow puncta, and after fusion, autolysosomes are shown by only mCherry signals as red-only puncta because GFP loses its fluorescence in acidic pH. Compared with control PNs, VEGF siRNA-treated cells showed significantly increased yellow puncta (autophagosomes) and decreased mCherry-only puncta (autolysosomes), indicating that VEGF depletion inhibited the autophagosome-lysosome fusion (Fig. 6g).

Sphingosine accumulation can induce defective calcium release from the acidic compartment such as lysosome, which inhibits fusion of lysosome with other organelles⁴. As shown in Supplementary Figs 2g and 3h, decreased VEGF levels caused sphingosine accumulation in WT PNs. Thus, we hypothesized that defective lysosomal calcium release by VEGF-mediated sphingosine accumulation disturbs autophagosome-lysosome fusion and evokes the abnormal autophagosomes' amassment. To test this hypothesis, we used the weaker sarcoplasmic reticulum ATPase antagonist curcumin, a natural product derived from turmeric²⁶, which correct sphingolipid imbalance by increasing the cytosolic calcium release⁴. Importantly, abnormal sphingolipid levels in the VEGF siRNA-treated PNs were normalized after curcumin treatment (Fig. 6h). We also observed significantly decreased protein level of abnormal autophagic markers (Fig. 6i) and increased neuronal survival (Fig. 6j) in the VEGF-knockdown PNs after curcumin treatment compared with PNs with VEGF knockdown alone. Similar results were observed in the VEGF shRNA-treated mice after curcumin injection (Supplementary

Fig. 6). To further examine these effects, we analysed calcium homeostasis in the primary cultured PNs derived from WT, NP-C and VEGF/NP-C mice. To specifically assess the lysosomal calcium content, we used Gly-Phe β -naphthylamide (GPN), which osmotically lyses cathepsin-containing lysosome⁴. We observed a reduction in NP-C PNs' calcium release from lysosome compared with WT PNs, consistent with our previous study⁷. Notably, this reduction was corrected in VEGF/NP-C PNs (Fig. 6k). As expected, abnormal sphingosine accumulation was reduced in VEGF/NP-C cells by restoration of SphK activity (Fig. 6l). Moreover, VEGF/NP-C PNs showed decreased autophagosome (yellow LC3 puncta) accumulation (Fig. 6m). Decreased autophagosomes in the VEGF/NP-C PNs were further confirmed by EM analysis (Fig. 6n). The survival of PNs was also significantly increased in the VEGF/NP-C (Fig. 6o). Together, these findings show that inactivated VEGF/SphK pathway in NP-C PNs causes sphingosine accumulation and this amassment inhibits autophagosome-lysosome fusion by disturbance of calcium homeostasis.

VEGF rescues autophagic defects in patient-specific cells. To further validate our observation regarding VEGF treatment in NP-C mice, we studied effects of VEGF on SphK activity in human NP-C fibroblasts. Human NP-C fibroblasts cocultured with human BM-MSCs, VEGF^{tg} BM-MSCs or treated with recombinant VEGF showed significantly increased SphK activity, decreased sphingosine and elevated S1P (Supplementary Fig. 7a–c). Increased LC3-II levels and p62 accumulation in NP-C fibroblasts were reduced by VEGF treatment (Supplementary Fig. 7d,e). VEGF-treated NP-C fibroblasts also showed increased calcium release and decreased autophagosome accumulation (as judged by yellow LC3 puncta) compared with non-treated NP-C fibroblasts (Supplementary Fig. 7f,g). Lysosomal exocytosis is necessary to affect clearance of stored intracellular lipids and ameliorates the endolysosomal lipid storage phenotype in NP-C cells²⁷. To determine whether VEGF directly induced lysosomal exocytosis, the culture media of normal and NP-C fibroblasts treated with or without VEGF were analysed for the presence of the lysosomal enzyme β -hexosaminidase as a marker for lysosomal content secretion. In all groups, the activity of β -hexosaminidase was not significantly elevated at the indicated times (Supplementary Fig. 7h). The low-level appearance of β -hexosaminidase in the culture media of fibroblasts is not a result of generalized cell lysis, since the levels of lactate dehydrogenase (LDH) in the media remained unchanged in all groups for the duration of the assay (Supplementary Fig. 7h). These results suggested that the ability of

Figure 7 | VEGF ameliorates sphingolipid imbalance in NP-C iPSC neurons. (a) Left, normal, hNPC-3 and hNPC-17 iPSCs generated nestin-positive neuroprogenitor cells (scale bar, 50 μ m). Right, representative images of immunocytochemical staining the β -III tubulin following neural differentiation (scale bar, 50 μ m). (b) hNPC-3 and hNPC-17 neurons were treated with human BM-MSCs, VEGF^{tg} BM-MSCs or recombinant VEGF (10 ng ml⁻¹). Three days after treatment, VEGF levels were measured in cell lysates. (c–f) SphK activity (c), sphingosine (d), S1P (e) and sphingomyelin (f) were measured in normal iPSC neurons and hNPC neurons with or without treatment. (g) Filipin staining of unesterified cholesterol in hNPC-3 neurons with or without treatment of recombinant VEGF for 3 days (scale bar, 50 μ m). Quantification of filipin fluorescence intensities normalized to normal neurons. Unesterified cholesterol levels in normal iPSC neurons and hNPC neurons with or without treatment were measured ($n = 6$ per group). (h) Effect of the VEGFR2 inhibitor on VEGF mediated sphingolipid modulation. hNPC-3 neurons were pretreated with PTK787 at 10 μ M for 1 day and were treated for 3 days with 10 ng ml⁻¹ VEGF and then assayed for SphK activity, sphingosine and S1P ($n = 7$ per group). (i,j) Effect of NPC1 knockdown on sphingolipid factors in normal iPSC neurons. (i) Three days after NPC1 siRNA transfection, we measured the levels of NPC1 mRNA and VEGF expression. (j) SphK activity, sphingosine and S1P were measured in normal iPSC neurons treated with control or NPC1 siRNA (control, $n = 7$; NPC1 siRNA, $n = 9$). (k) Effect of VEGF knockdown on sphingolipid factors in normal iPSC neurons. Three days after VEGF siRNA transfection, we measured the levels of VEGF mRNA, SphK activity, sphingosine and S1P in normal iPSC neurons ($n = 7$ per group). (l) Effect of a specific SphK1 inhibitor on sphingolipid factors in normal iPSC neurons. Normal neurons were treated with or without 20 μ M SKI-1 for 6 h. Lipids were extracted and sphingosine, S1P and unesterified cholesterol levels were determined ($n = 6$ per group). b–h, one-way analysis of variance, Tukey's *post hoc* test. i–l, Student's *t*-test. * $P < 0.05$, ** $P < 0.01$, *** $P < 0.005$. All error bars indicate s.e.m.



VEGF to reduce sphingosine storage in NP-C cells was not due to lysosomal exocytosis.

The recent developments in induced pluripotent stem cells (iPSCs) and iPSC-derived neurons have allowed investigation of pathogenesis of neurological diseases *in vitro*. To explore whether the observed effects of VEGF we describe above were similar in NP-C human neurons, we established human NP-C iPSCs (hNPC-3, 6, 17) by transduction of human NP-C fibroblasts with retroviruses encoding *OCT4*, *SOX2*, *KLF4* and *c-MYC* similar to previous studies^{28–30}. Analysis of NP-C iPSCs (hNPC-3) revealed typical characteristics of pluripotent stem cells: similar morphology to embryonic stem cells (ES cells), expression of pluripotent markers including SSEA-4, Tra-1-60 and Tra-1-81, normal chromosomal number and genomic structure, silencing of retroviral transgene and reactivation of genes indicative of pluripotency (Supplementary Fig. 8a–c). The differentiation ability of NP-C iPSCs was also confirmed *in vivo* by teratoma formation (Supplementary Fig. 8d). We analysed SphK activity and sphingolipid levels in the normal iPSC and NP-C iPSC lines. NP-C iPSC lines exhibited decreased SphK activity, increased sphingosine accumulation and decreased S1P levels compared with normal iPSCs (Supplementary Fig. 8e).

Next, human neurons were induced from the hNPC-3, hNPC-17 and normal iPSC. Early-differentiating cells expressed nestin and differentiated cells expressed neuron-specific β -III tubulin (Fig. 7a). These NP-C neurons also exhibited phenotypes seen in human NP-C samples, including abnormal VEGF levels and sphingolipid metabolism (Fig. 7b–e). To confirm the effects of VEGF in human NP-C neurons, the hNPC-3- or hNPC-17-derived neurons were cocultured with human or VEGF^{tg} BM-MSCs, or treated with recombinant VEGF. We found that all treated groups exhibited increased VEGF, elevated SphK activity, decreased sphingosine accumulation and increased S1P levels (Fig. 7b–e). Sphingomyelin and unesterified cholesterol levels were also significantly decreased in VEGF-treated NP-C neurons (Fig. 7f,g). We also pretreated NP-C neurons with PTK787 before VEGF treatment. We found that SphK activity and other sphingolipid metabolites in NP-C neurons were mediated by interactions of VEGF and its receptor VEGFR2 in these iPSC-derived NP-C neurons (Fig. 7h).

To reconfirm the *in vitro* mechanism whereby there is a direct relationship between *NPC1*, VEGF and SphK activity in human neurons, we treated normal iPSC neurons with *NPC1* and VEGF siRNA (Fig. 7i–k) and determined changes in various sphingolipid factors. *NPC1* siRNA decreased VEGF expression and SphK activity (Fig. 7i,j). VEGF siRNA also strongly inactivated SphK levels (Fig. 7k). Both siRNA treatments led to changed levels of

sphingosine and S1P, similar to NP-C neurons (Fig. 7j,k). To determine whether reduction in SphK activity affected sphingolipid factors and unesterified cholesterol in iPSC neurons similar to those in classical NP-C cells, we treated the normal iPSC neurons with a specific SphK1 inhibitor, SK1-I. We found that inhibition of SphK activity increased sphingosine and unesterified cholesterol accumulation and decreased cellular S1P (Fig. 7l).

We also examined whether NP-C neurons exhibited abnormal autophagy. NP-C neurons had significantly higher abnormal autophagic markers than normal neurons (Fig. 8a). VEGF treatment significantly decreased the protein level of abnormal autophagic markers in NP-C neurons (Fig. 8a). Similar to previous results (Supplementary Fig. 7), VEGF-treated NP-C neurons showed increased calcium release and decreased autophagosome accumulation, suggesting that VEGF elevates autophagosome–lysosome fusion (Fig. 8b–d). Consistent with the restored autophagy flux, cell survival was also significantly improved in VEGF-treated NP-C neurons (Fig. 8e). Collectively, these results confirm that defective autophagy by abnormal VEGF/SphK pathway and sphingosine levels in NP-C mice and human fibroblasts also occur in NP-C patient neurons, and replenishment of VEGF is able to ameliorate autophagy defect by correction of sphingolipid imbalance in the NP-C patient cells.

Discussion

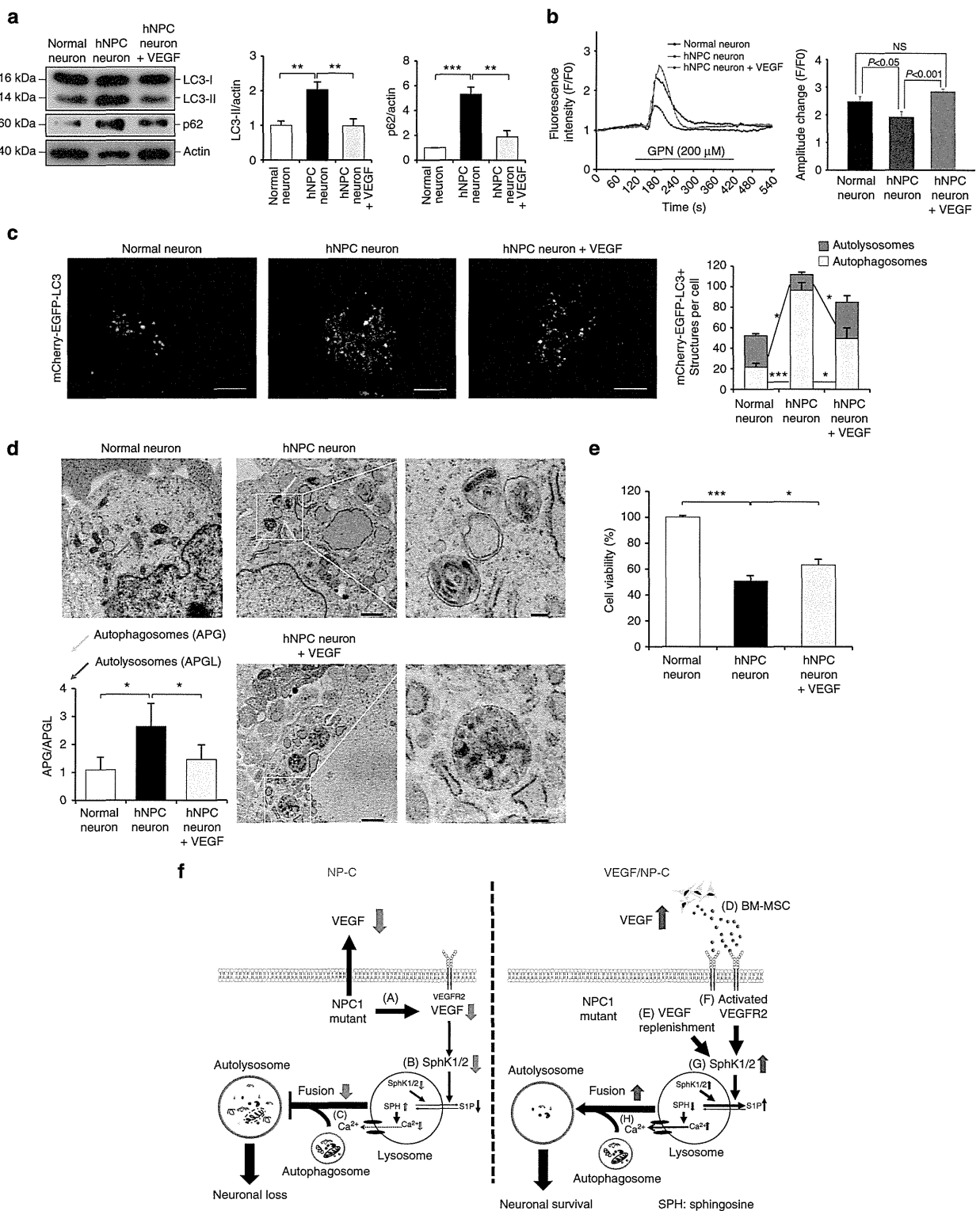
NP-C patients and mice exhibit progressive neuronal loss, mainly of cerebellar PNs, but the mechanism is largely unknown. Recent studies have shown that inactivation of *NPC1* caused abnormal autophagy and the defect may contribute to PN loss in NP-C²². Loss of *NPC1* function leads to trapping of lipids within aberrant membrane compartments, and this may induce a ‘lipid-starvation response’ analogous to the well-characterized autophagic response to amino-acid deprivation³¹. In addition, destructive autophagy in NP-C PNs may also be stimulated hormonally via neurosteroids. Neurosteroids might inhibit autophagy in PNs and when their synthesis is severely decreased, as in NP-C³², autophagic cell death might ensue. Similar to previous results^{22,33}, we found that the impaired autophagic flux in NP-C was associated with decreased autophagosome–lysosome fusion, and that this defect led to PNs loss.

Recent studies have also demonstrated that cholesterol, sphingomyelin and GSL storage are downstream events in NP-C disease pathogenesis caused by sphingosine storage, leading to altered acidic compartment calcium levels⁴. They

Figure 8 | VEGF rescues the autophagic defects in NP-C iPSC neurons. (a) Western blot analysis of LC3 and p62 in normal and NP-C iPSC-derived neurons treated with or without 10 ng ml^{−1} recombinant VEGF (normal, *n* = 6; hNPC, *n* = 7; and VEGF-treated hNPC, *n* = 7). (b) Left, representative traces showing intracellular [Ca²⁺] changes monitored in single fluo-4-loaded normal and NP-C iPSC neurons treated with or without recombinant VEGF (10 ng ml^{−1}). Right, maximal peak fluorescence changes were determined as the differences between basal and the maximum fluorescence, on addition of 200 μ M GPN (*n* = 10 cells per group). (c) Fluorescence staining and quantification of autophagosomes (mCherry⁺-EGFP⁺-LC3) and autolysosomes (mCherry⁺-EGFP[−]-LC3) in normal and NP-C iPSC neurons after recombinant VEGF treatment (normal, *n* = 7; hNPC, *n* = 8; and VEGF-treated hNPC, *n* = 8; scale bar, 10 μ m). (d) EM images and quantification data of normal and NP-C iPSC-derived neurons after 10 ng ml^{−1} VEGF treatment (*n* = 5 per group; low-magnification scale bar, 1 μ m; high-magnification scale bar, 200 nm). (e) Quantification of cell viability (normal, *n* = 5; hNPC, *n* = 6; and VEGF-treated hNPC, *n* = 6). (f) Model of VEGF-mediated SphK activation in NP-C neurons. (A,B) In NP-C cells, sphingosine accumulation is increased due to defective SphK activity together with decreased VEGF caused by mutated *NPC1* and defective uptake via VEGFR2. (C) Abnormal sphingosine accumulation decreases calcium release from lysosomes and the reduction in calcium release causes an autophagic defect by inhibiting autophagosome–lysosome fusion. Eventually, these defects cause loss of cerebellar neurons. (D,E) When NP-C neurons are exposed to BM-MSCs or pure VEGF, the cells exhibit elevated intracellular levels of VEGF (F), which induces VEGFR2-mediated activation of SphK in the cytosol and lysosome. (G) This activation leads to decreased sphingosine accumulation and increased S1P levels. (H) Reduced sphingosine accumulation results in improved autophagosome–lysosome fusion by correction of calcium homeostasis. Finally, this restoration prevents neuronal loss in NP-C. **a–e**, one-way analysis of variance, Tukey’s *post hoc* test. **P* < 0.05, ***P* < 0.01, ****P* < 0.005. All error bars indicate s.e.m.

have determined the chronology of events after inactivation of NPC1. In a drug-induced NP-C cellular model, sphingosine storage in the acidic compartment led to calcium depletion in these organelles, which then resulted in cholesterol, sphingomyelin and GSL storage in these compartments. Therefore, sphingosine storage might be an initiating factor in

NPC1 disease pathogenesis that causes altered calcium homeostasis, leading to the secondary storage of sphingolipids and cholesterol, although additional studies are required. Similarly, we found that VEGF-mediated sphingosine modulation also significantly decreased sphingomyelin and unesterified cholesterol levels. Therefore, we suggest that



replenishment of VEGF is able to ameliorate accumulation of sphingomyelin and unesterified cholesterol by reducing sphingosine accumulation in the NP-C. Similar to sphingosine accumulation, cholesterol accumulation also induced changes in autophagy-lysosome function in PNs and lead to death of these cells. In NP-C mouse brain, combined LC3 immunofluorescence and filipin staining showed that LC3 accumulated within filipin-labelled cholesterol clusters inside PNs³⁴. These results provide strong evidence that cholesterol accumulation-induced changes in autophagy-lysosome function are closely associated with neurodegeneration in NP-C. Therefore, we suggest that reduced PN survival in NP-C may be due to impaired autophagic flux by VEGF/SphK pathway-mediated sphingosine accumulation and secondary storage of cholesterol.

Despite extensive data supporting the modulating effect of VEGF on SphK in NP-C, the clinical effectiveness of VEGF-mediated therapy in the NP-C mouse model was the modest. There are several potential explanations for this finding. First, it must be recognized that in these animal model experiments the primary lesion in the *Npc1* gene and protein remains in the treated mice, and thus correction of their sphingolipid imbalance via VEGF may only slow progression and require additional, combinational therapies to achieve a more complete clinical effect. In addition, VEGF may not be the only factor regulating sphingolipid metabolism in NP-C, as suggested by the fact that the sphingolipid levels were improved, but not normalized, in the treated cells and mice. Finally, the methods used to introduce VEGF into the brain of the NP-C mice may need to be improved, and there are considerable research underway exploring different approaches to introducing proteins such as VEGF into the central nervous system^{35,36}. Indeed, small molecules may also be developed in the future that modulate VEGFR2 leading to SphK enhancement, or even small molecules that work on SphK directly. Despite the limitations of these animal model studies, however, the findings reported in the manuscript describe a novel pathogenic mechanism in NP-C and reveal a potential approach for the therapy via the VEGF/SphK pathway.

In summary, the data presented here show that VEGF and SphK activities are reduced in both NP-C mouse PNs and patient-specific cells, and that correction of this activity by VEGF (released from BM-MSCs or added directly into the CNS) can reduce NP-C pathological changes via increasing autophagic degradation (Fig. 8f). Thus, VEGF is a therapeutic candidate for NP-C that influences sphingosine storage via SphK modulation, suggesting that enhancing SphK activity is a potential therapeutic intervention for this disorder.

Methods

Mice. A colony of Balb/c *Npc1*^{nh} mice has been maintained and the genotype of each mouse was determined by PCR using forward (5'-GGTGCTGGACAGCCA AGTA-3') and reverse primer (5'-GATGGTCTGTTCTCCCATG-3')³⁷. VEGF-overexpressing transgenic mice¹⁴ were bred with NP-C mice to generate VEGF/NP-C (*VEGF*^{tg}/*Npc1*^{-/-}) mice. Four-week-old mice were used for transplantation of BM-MSCs and microspheres. We choose the block randomization method to allocate the animals to experimental groups. For the cerebellar transplantation⁷, the injections were carried out using a glass capillary (1.2 × 0.6 mm). The injection coordinates were 5.52 mm posterior to bregma and injection depth was 2.50 mm. In some experiments, mice were treated with the VEGFR inhibitor PTK787/ZK222584 (PTK787; 100 mg kg⁻¹, Selleck Chemicals) or PBS vehicle control by oral gavage once a day for 3 days. PTK787 is a potent and relatively selective inhibitor of all VEGF receptor tyrosine kinases, with greater activity against VEGFR2¹⁷. Three-week-old WT mice were treated with VEGF shRNA and curcumin (Supplementary Fig. 6a). Eight-week-old male SCID Beige mice (Charles River Laboratories) were used for teratoma formation assay. To eliminate the bias, we were blinded in experimental progress such as data collection and data analysis. Mice were housed at a 12 h day-night cycle with free access to tap water and food pellets. Mouse studies were approved by the Kyungpook National University Institutional Animal Care and Use Committee.

Cell isolation and culture. Human *NPC1*-mutant and control fibroblasts (GM03123 and GM05399, respectively) were acquired from the Coriell Institute and were used at passages 10–15. Primary PN cultures were prepared from the cerebellum of individual embryonic day 18 fetuses⁷. The cerebellum was dissociated using the Nerve-Cell Culture System (Sumitomo Bakelite) and plated in the PN culture media⁷. To isolate mouse BM-MSCs⁶, bone marrow was harvested from tibias and femurs of 4- to 6-week-old Balb/c or VEGF-overexpressing transgenic mice, and single-cell suspensions were obtained using a 40-μm cell strainer (BD Biosciences). Cells containing MesenCult MSC Basal Medium plus Supplements (Stemcell Technologies) were plated. Normal iPSC line (HPS0063) was obtained from the RIKEN Bioresource Center³⁸. Human BM-MSCs were kindly provided by the Cell Therapy Center of Yonsei University. Informed consent was obtained from all subjects according to the ethics committee guidelines at the Yonsei University Severance Hospital. For some experiments, cells were treated with human recombinant VEGF (R&D Systems), human and mouse SMART pool VEGF siRNA (Dharmacon), human and mouse SMART pool NPC1 siRNA (Dharmacon) or scrambled sequence siRNA control (Dharmacon). NH₄Cl was used to inhibit autophagic flux. Curcumin (Sigma-Aldrich) was used to increase cytosolic calcium release. For the inhibition of VEGFR2 signal activation *in vitro*, cells were pretreated for 1 day with 10 μM of PTK787. For the inhibition of SphK1 activation *in vitro*, cells were pretreated for 6 h with 20 μM of SKI-1 (Enzo Life Sciences).

Indirect coculture of BM-MSCs. For the indirect coculture experiments, 1.0 μm pore size Millicell Hanging Cell Culture Inserts (Millipore) were placed on top of the previously plated cells. BM-MSCs were seeded onto the insert at a density of 3 × 10⁴ cells per insert. In this system there was no direct contact between cocultured cells and BM-MSCs.

SphK activity assays. SphK activity was followed as phosphorylation of (7-nitro-2-1,3-benzoxadiazol-4-yl)-d-erythro (NBD)-sphingosine (Avanti Polar Lipids) to NBD-S1P as described previously³⁹ with modification using a UPLC (ultra performance liquid chromatography) system (Waters). Quantification was achieved by comparison with NBD-S1P (Avanti Polar Lipids) standards. Cell and tissue lysates were prepared as previously described⁷. Values were expressed as percent of control.

Lipid extraction and sphingosine/S1P/sphingomyelin quantification. Samples were lysed in homogenization buffer containing 50 mM HEPES (Gibco), 150 mM NaCl (Sigma-Aldrich), 0.2% Igepal (Sigma-Aldrich) and protease inhibitor (Calbiochem)⁷. To quantify the sphingosine, S1P and sphingomyelin levels, the dried lipid extract was resuspended in 0.2% Igepal CA-630. Four microlitres of the lipid extracts was added into 20 μl of NDA derivatization reaction mixture (25 mM borate buffer, pH 9.0, containing 2.5 mM each of NDA and NaCN). The reaction mixture was diluted 1:3 with ethanol, incubated at 50 °C for 10 min and centrifuged (13,000g for 5 min). An aliquot (30 μl) of the supernatant was then transferred to a sampling glass vial and 5 μl was applied onto an UPLC system for analysis. The fluorescent sphingosine or S1P derivatives were monitored using a model 474 scanning fluorescence detector (Waters). Quantification of the sphingosine, S1P and sphingomyelin peaks were calculated from sphingosine, S1P and sphingomyelin standard calibration curves using the Waters Millennium software.

Cytokine antibody array. RayBio Custom Mouse Cytokine Antibody Arrays (RayBiotech) were employed for assay of cell culture supernatants from coculture experiments according to the manufacturer's instructions.

ELISA. VEGF protein levels were assayed by using a Mouse and Human VEGF Quantikine kit (R&D Systems) according to manufacturer's instructions.

Immunofluorescence staining. For the immunofluorescence staining, cells and brain sections were blocked with PBS containing 5% normal goat serum (Vector Laboratories), 2% BSA (Gibco) and 0.4% Triton X-100 (Sigma-Aldrich). In the same buffer solution, the cells and sections were then incubated for 24 h with primary antibodies. The following antibodies were used: anti-VEGF (rabbit, 1:500, Invitrogen, ab39250), anti-calbindin (rabbit, 1:500, Chemicon, ab82812 and mouse, 1:500, Abcam, ab9481), anti-S1P (mouse, 1:400, Alfresa Pharma, 274594052), anti-LC-3B (rabbit, 1:200, Cell Signaling Technologies, 3868S), anti-active caspase-3 (rabbit, 1:50, Chemicon, AB3623), anti-β-III tubulin (mouse, 1:400, Chemicon, MAB1637), anti-nestin (mouse, 1:400, Chemicon, MAB353), anti-SSEA-4, TRA-1-60 and TRA-1-81 (mouse, 1:100, Chemicon, MAB4304, MAB4360 and MAB4381). The cells and sections were analysed with a laser scanning confocal microscope equipped with Fluoview SV1000 imaging software (Olympus FV1000) or with an Olympus BX51 microscope. Metamorph software (Molecular Devices) was used to calculate the average intensity.

Filipin staining. Cells and cerebellar sections were fixed with 4% paraformaldehyde for 15 min, washed with PBS and incubated for 30 min with 100 μg ml⁻¹ filipin (Polysciences) in PBS. Cells and cerebellar sections were washed twice with PBS for 5 min. The averaged intensities were analysed as described above.

Amplex red assay. The cells and cerebellar tissues were lysed with lysis buffer (50 mM phosphate buffer, 500 mM NaCl, 25 mM cholic acid and 0.5% Triton X-100). The unesterified cholesterol was determined using the Amplex Red Cholesterol Assay Kit (Molecular Probes) according to the manufacturer's instructions. After incubation for 30 min at 37 °C, the fluorescence intensities were measured on a microplate reader (Molecular devices) equipped with a filter set for excitation and emission at 560 ± 10 nm and 590 ± 10 nm, respectively. The cholesterol content was calculated with a cholesterol standard curve. Cellular cholesterol content was normalized to protein content.

GSL analysis. Cerebellum from 6-week-old mice was homogenized with four volumes of ice-cold water in an all-glass Potter-Elvehjem homogenizer; 250 µl of homogenate (50 mg of wet tissue) was extracted by addition of 1.2 ml of methanol and 2 ml of chloroform. After incubation of the samples at 37 °C for 1 h, 1 ml of methanol was added, and the extracts were centrifuged at 2,000 g for 10 min. The pellet was re-extracted with 2 ml of chloroform/methanol/water (1/2/0.8, v/v/v) at 37 °C for 2 h. The combined supernatants were concentrated by Speed-Vac, and the dried samples were dissolved in 2 ml of methanol and saponified. After neutralization, samples were diluted with 2 ml of water and desalted using OASIS HLB 1 cc extraction cartridges (Waters). Thin-layer chromatography was performed using HPTLC (Merck) and developed with chloroform/methanol/0.02% CaCl₂ (5:4:1, v/v). After staining with orcinol-sulfuric acid, GSLs were identified by comparing their R_f to those of authentic GSL standards.

Isolation of cytosolic-enriched and lysosome-enriched fractions. Cerebellum from 6-week-old mice was washed twice with cold PBS, and then cytosolic-enriched and lysosome-enriched fractions were extracted. Lysosomes were isolated on sucrose gradient by using a lysosome isolation kit from Sigma-Aldrich. β-N-acetylglucosaminidase activity quantifications (Sigma-Aldrich), according to the manufacturer instructions, was used to identify lysosomal fractions. Cytosolic-enriched fractions (hydrophilic) were extracted using Mem-PER Membrane Protein Extraction Kit (Pierce) containing protease inhibitor mixture.

β-Hexosaminidase assays. Human fibroblasts were incubated with recombinant VEGF (10 ng ml⁻¹) and 2 mM mannose-6-phosphate at 37 °C. At the indicated time points, an aliquot of media was removed and assayed for β-hexosaminidase activity at 37 °C and pH 4.4 by using the synthetic substrate 4-methylumbelliferyl-N-acetyl-glucosaminide (Sigma-Aldrich). After the last time point, cells were lysed and an aliquot of the lysate assayed for β-hexosaminidase activity to determine the total enzyme activity of each sample. Enzyme activities were expressed as a percentage of the total enzyme activity found in the lysate. To confirm cell viability, LDH assays were performed, using an aliquot of culture medium taken at the indicated time points by an LDH assay kit (Sigma-Aldrich).

Cell viability. Viability of human iPSC-derived neurons was quantified by using WST-1 (Roche). Briefly, human iPSC-derived neurons were seeded on to 24-well plates at a density of 1 × 10⁴ cells per well. Recombinant VEGF (10 ng ml⁻¹) was added to culture media, and the cells were incubated for an additional 72 h. WST-1 solution was then added to each well, and the cells were further incubated. After 4 h, the absorbance was measured with a plate reader at 440 nm.

Laser capture microscopy. LCM was performed by the P.A.L.M. Laser Pressure Catapult system (Zeiss Instruments) using standard procedures. Briefly, cerebella were immediately frozen into a block of tissue freezing medium (Electron Microscopy Sciences). The frozen blocks were cut into 8-µm-thick sections that were then mounted on Arcturus PEN membrane glass slides (Applied Biosystems). The slides were then stained with 0.1% crystal violet (Sigma-Aldrich) and viewed with a Zeiss Observer Z1 inverted light microscope using a ×40 objective. The Zeiss P.A.L.M. device uses a ultraviolet laser beam focused on a selected area of tissue. The collecting cap was placed over the targeted PNs, and by applying a single pulse of laser the targeted cells were catapulted into the collection cap. Total RNA from the isolated cells was extracted with the RNeasy Micro Kit (Qiagen) and then subjected to T7 RNA polymerase-based linear amplification using the Mesage BOOSTER kit for quantitative PCR (Epicentre).

Reverse-transcriptase PCR and quantitative real-time PCR. The RNeasy Lipid Tissue Mini kit or RNeasy Plus Mini Kit (Qiagen) was used for extraction of RNA from brain homogenates and cell lysates. Complementary DNA was synthesized from 5 µg of total RNA using the cDNA Synthesis Kit (Clontech) according to the manufacturer's protocol. Quantitative real-time PCR was performed using a Corbett research RG-6000 real-time PCR instrument. Used primers are described in Supplementary Table 1.

Behavioural studies. We performed behavioural studies to assess mouse balance and coordination by measuring the amount of time the animal was able to remain on a longitudinally rotating rod. Briefly, the Rota-rod apparatus (Ugo Basile) was set to an initial speed of 4 r.p.m., and the acceleration was increased by 32 r.p.m.

every 25–30 s. Scores were registered every 3 days, and three independent tests were performed at each measurement.

Western blotting. Samples were lysed in RIPA buffer (Cell signaling Technologies), then subjected to SDS-PAGE and transferred to a nitrocellulose membrane. Membranes were blocked with 5% milk, incubated with primary antibody and then incubated with the appropriate horseradish peroxidase-conjugated secondary antibody. Primary antibodies to the following proteins were used: LC3 (rabbit, 1:1,000, 4108S) Beclin-1 (rabbit, 1:1,000, 3738S), p62 (rabbit, 1:1,000, 5114S), rab5 (rabbit, 1:1,000, 3547S), rab7 (rabbit, 1:1,000, 9367S), TFEB (rabbit, 1:1,000, 4240S; all from Cell Signaling Technologies), Lamp1 (rabbit, 1:1,000, Abcam, AB24170), TFEB (rabbit, 1:500, Novus, NBP1-67872), cathepsin D (goat, 1:500, R&D Systems, BAF1029) and β-actin (1:1,000, Santa Cruz, SC-1615). We carried out densitometric quantification using the ImageJ software (US National Institutes of Health). Full scans of western blots are provided in Supplementary Fig. 9.

Measurement of activity of cathepsin D. Enzyme activity of cathepsin D was determined with cathepsin D activity fluorometric assay kit according to the manufacturer's protocol (Abcam).

LysoTracker labelling and quantification. LysoTracker red (Invitrogen) was used at a final concentration of 75 nM. H₂O₂- and NH₄Cl-treated cells were used as positive and negative controls, respectively. The cells were trypsinized, resuspended in PBS and analysed on a FACS Calibur using FACSDiva software (Becton Dickinson).

Electron microscopy. Brain tissues and cells were fixed in 3% glutaraldehyde/0.1 M phosphate buffer, pH 7.4, and postfixed in 1% osmium tetroxide in Sorensen's phosphate buffer. After dehydration in ethyl alcohol, the tissues and cells were embedded in Epon (Electron Microscopy Sciences). Samples were cut serially and placed on copper grids and analysed using transmission electron microscope (Tecnai). Images were captured on a digital camera and Xplore3D tomography software.

Analysis of autophagic flux with mCherry-EGFP-LC3 reporter. mCherry-EGFP-LC3B (plasmid 22418) was acquired from Addgene. Transfection was performed using Lipofectamine2000 (Invitrogen) according to the manufacturer's protocol. Autophagosome and autolysosome were quantified by image J software.

Intracellular Ca²⁺ concentration. Changes in [Ca²⁺]_i were determined by a confocal laser scanning microscope using a C-apochromat ×40 objective (1.2 numerical aperture). The excitation wavelength for the detection of Ca²⁺ was 488 nm, and the emission wavelength was 516 nm. The fluorescent images were generated at 25 °C and analysed using LSM5 EXCITER software (Carl Zeiss). For the Ca²⁺ measurements, cells were loaded with the Ca²⁺-sensitive dye fluo-4/acetoxymethyl ester (3 µmol l⁻¹; Molecular Probes, Eugene, OR, USA) in Krebs-Ringer phosphate-HEPES (KRPH) buffer containing 0.2% BSA (pH 7.4) for 30 min. The cells were incubated for 30 min in a dye-free solution to allow esterase cleavage of the fluo-4/acetoxymethyl ester to liberate fluo-4. After the establishment of a stable baseline [Ca²⁺]_i level, the cells were stimulated with 200 µM GPN for 5 min. GPN was applied using a flow system with a flow rate of ~1 ml min⁻¹. The images were collected at 5 s intervals, and the results were plotted as the change in fluorescence intensity expressed in arbitrary units. The magnitude was calculated as the change in fluorescence intensity expressed as a percentage of the basal fluorescence intensity (F₀). The area under the curve was calculated using Microcal Origin software version 7.0 (Northampton, MA, USA).

Lentiviral shRNA-mediated depletion of VEGF and NPC1. We cloned VEGF and NPC1 shRNAs into lentiviral vector plasmid CS-CDF-CG-PRE. The following short hairpin sequences were used: 5'-GATGTGAATGCAGACCAAGA-3' (SABiosciences-Qiagen; KM03041N; VEGF-shRNA #4); 5'-AGTCCAG-TACGGCTCCAA-3' (SABiosciences-Qiagen; KM03041N; NPC1-shRNA #3); and 5'-GGAATCTCATTGATGCATAC-3' (SABiosciences-Qiagen; negative control shRNA). The shRNA-expressing lentiviruses were produced by transient transfection of 293T cells⁴⁰. Virus-containing media were collected, filtered and concentrated by ultracentrifugation at 50,000 g for 2 h and resuspended in PBS. Viral titres were measured by serial dilution on 293T cells, followed by flow cytometry analysis after 48 h. The titre of the virus used ranged between 2 and 5 × 10⁹ plaque-forming units per ml. Three µl of lentiviruses was administered into the cerebellum of 4-week-old mice by stereotaxic injection 3 days before analysis as previously described⁷.

Preparation of VEGF-loaded microspheres. VEGF-loaded poly(lactic-co-glycolic acid) (PLGA) microspheres were prepared using the method of water-in-oil-in-water emulsification⁴¹. Briefly, human recombinant VEGF-A (R&D Systems) in powder form was dispersed in PLGA (50:50 lactic to glycolic acid copolymer ratio

with a molecular weight of 40,000–75,000) solution in CH_2Cl_2 using a homogenizer. Polyvinylalcohol (PVA) solution (1%) was added to this mixture and homogenized. This emulsion was poured into a 0.1% PVA solution and stirred for 1 h. The hardened microspheres were centrifuged, filtered and washed and subsequently dried for 24 h under vacuum.

Maintenance and generation of iPSCs. Established iPSC and ES cells were maintained on mitomycin C-treated mouse embryonic fibroblasts (MEFs) in complete ES medium composed of DMEM (Sigma-Aldrich) supplemented with 20% knockout serum replacement, 5 ng ml^{-1} recombinant human basic fibroblast growth factor (FGF) (Peprotech), 20 mM HEPES buffer (pH 7.3), 0.1 mM 2-mercaptoethanol, 0.1 mM non-essential amino acids, 2 mM L-glutamine and 100 U ml^{-1} penicillin/streptomycin (all other materials were from Gibco). NP-C iPSCs were established from NP-C patient skin fibroblasts (GM03123, Coriell Institute)^{42,43}. In brief, NP-C fibroblasts were seeded at 3×10^5 cells in 60-mm² dish coated with gelatin (Sigma-Aldrich). On day 1, the vesicular stomatitis virus G glycoprotein (VSV-G)-pseudotyped retroviral vector carrying *OCT4*, *SOX2*, *KLF4* and *c-MYC* was added to the fibroblasts. On day 2, cells were subjected to the same transduction procedures and harvested 24 h later. Transduced cells were replated on MEF layers in 100-mm² dish containing the fibroblast medium. On the next day, the medium was changed to complete ES medium with 0.5 mM valproic acid (Sigma-Aldrich), and thereafter changed every other day. After 20 days, ES-like colonies appeared and were picked up to be reseeded on new MEF layers. Cloned ES-like colonies were subjected to further analysis.

In vitro differentiation of human iPSCs. Neural differentiation of iPSCs was performed⁴⁴. Briefly, iPSC colonies were detached from feeder layers and cultured in suspension as embryoid body for about 30 days in bacteriological dishes. EBs were then enzymatically dissociated into single cells and the dissociated cells cultured in suspension in serum-free hormone mix media^{44,45} for 10–14 days to allow the formation of neurospheres. Neurospheres were passaged repeatedly by dissociation into single cells, followed by culture in the same manner. Typically, neurospheres between passages 3 and 8 were used for analysis. For terminal differentiation, dissociated neurospheres were allowed to adhere to poly-L-ornithine- and laminin-coated coverslips and cultured for 10 days.

Alkaline phosphatase staining. Alkaline phosphatase staining was performed using an ES-alkaline phosphatase detection kit (Chemicon) according to manufacturer's recommendations.

Teratoma formation and histological analysis. Established iPSCs were prepared at 1×10^7 cells ml^{-1} in PBS. Suspended cells ($1\text{--}3 \times 10^6$) were injected into testes of anaesthetized male SCID Beige mice. Eight weeks after transplantation, mice were sacrificed and tumours were dissected. Tumor samples were fixed in 10% formalin and embedded in paraffin. Sections were stained with hematoxylin and eosin.

Statistical analysis. Comparisons between two groups were performed with Student's *t*-test. In cases where more than two groups were compared to each other, a one-way analysis of variance was used, followed by Tukey's honestly significant difference (HSD) test. Comparisons of overall survival were performed using a log-rank test. All statistical analysis was performed using SPSS statistical software. $P < 0.05$ was considered to be significant.

References

- Vanier, M. T. & Millat, G. Niemann-Pick disease type C. *Clin. Genet.* **64**, 269–281 (2003).
- Vanier, M. T. Lipid changes in Niemann-Pick disease type C brain: personal experience and review of the literature. *Neurochem. Res.* **24**, 481–489 (1999).
- Blom, T., Li, Z., Bittman, R., Somerharju, P. & Ikonen, E. Tracking sphingosine metabolism and transport in sphingolipidoses: NPC1 deficiency as a test case. *Traffic* **13**, 1234–1243 (2012).
- Lloyd-Evans, E. *et al.* Niemann-Pick disease type C1 is a sphingosine storage disease that causes deregulation of lysosomal calcium. *Nat. Med.* **14**, 1247–1255 (2008).
- Bae, J. S. *et al.* Bone marrow-derived mesenchymal stem cells promote neuronal networks with functional synaptic transmission after transplantation into mice with neurodegeneration. *Stem Cells* **25**, 1307–1316 (2007).
- Bae, J. S. *et al.* Neurodegeneration augments the ability of bone marrow-derived mesenchymal stem cells to fuse with Purkinje neurons in Niemann-Pick type C mice. *Hum. Gene Ther.* **16**, 1006–1011 (2005).
- Lee, H. *et al.* Bone marrow-derived mesenchymal stem cells prevent the loss of Niemann-Pick type C mouse Purkinje neurons by correcting sphingolipid metabolism and increasing sphingosine-1-phosphate. *Stem Cells* **28**, 821–831 (2010).
- Le Stunff, H., Peterson, C., Liu, H., Milstien, S. & Spiegel, S. Sphingosine-1-phosphate and lipid phosphohydrolases. *Biochim. Biophys. Acta* **1582**, 8–17 (2002).
- Shu, X., Wu, W., Mosteller, R. D. & Broek, D. Sphingosine kinase mediates vascular endothelial growth factor-induced activation of ras and mitogen-activated protein kinases. *Mol. Cell. Biol.* **22**, 7758–7768 (2002).
- Xia, P. *et al.* Tumor necrosis factor- α induces adhesion molecule expression through the sphingosine kinase pathway. *Proc. Natl Acad. Sci. USA* **95**, 14196–14201 (1998).
- Olivera, A. & Spiegel, S. Sphingosine-1-phosphate as second messenger in cell proliferation induced by PDGF and FCS mitogens. *Nature* **365**, 557–560 (1993).
- Edsall, L. C., Pirianov, G. G. & Spiegel, S. Involvement of sphingosine 1-phosphate in nerve growth factor-mediated neuronal survival and differentiation. *J. Neurosci.* **17**, 6952–6960 (1997).
- Spiegel, S. & Milstien, S. Sphingosine-1-phosphate: an enigmatic signalling lipid. *Nat. Rev. Mol. Cell Biol.* **4**, 397–407 (2003).
- Wang, Y. *et al.* VEGF overexpression induces post-ischaemic neuroprotection, but facilitates haemodynamic steal phenomena. *Brain* **128**, 52–63 (2005).
- Olsson, A. K., Dimberg, A., Kreuger, J. & Claesson-Welsh, L. VEGF receptor signalling - in control of vascular function. *Nat. Rev. Mol. Cell Biol.* **7**, 359–371 (2006).
- Cvetanovic, M., Patel, J. M., Marti, H. H., Kini, A. R. & Opal, P. Vascular endothelial growth factor ameliorates the ataxic phenotype in a mouse model of spinocerebellar ataxia type 1. *Nat. Med.* **17**, 1445–1447 (2011).
- Wood, J. M. *et al.* PTK787/ZK 222584, a novel and potent inhibitor of vascular endothelial growth factor receptor tyrosine kinases, impairs vascular endothelial growth factor-induced responses and tumor growth after oral administration. *Cancer Res.* **60**, 2178–2189 (2000).
- Foraker, J. E. *et al.* Cross-talk between human mesenchymal stem/progenitor cells (MSCs) and rat hippocampal slices in LPS-stimulated cocultures: the MSCs are activated to secrete prostaglandin E₂. *J. Neurochem.* **119**, 1052–1063 (2011).
- Ruiz de Almodovar, C. *et al.* Matrix-binding vascular endothelial growth factor (VEGF) isoforms guide granule cell migration in the cerebellum via VEGF receptor Flk1. *J. Neurosci.* **30**, 15052–15066 (2010).
- Sentilhes, L. *et al.* Vascular endothelial growth factor and its high-affinity receptor (VEGFR-2) are highly expressed in the human forebrain and cerebellum during development. *J. Neuropathol. Exp. Neurol.* **69**, 111–128 (2010).
- Folkman, J. Angiogenesis in cancer, vascular, rheumatoid and other disease. *Nat. Med.* **1**, 27–31 (1995).
- Ko, D. C. *et al.* Cell-autonomous death of cerebellar purkinje neurons with autophagy in Niemann-Pick type C disease. *PLoS Genet.* **1**, 81–95 (2005).
- Rubinstein, D. C. *et al.* In search of an 'autophagometer'. *Autophagy* **5**, 585–589 (2009).
- Settembre, C. *et al.* TFEB links autophagy to lysosomal biogenesis. *Science* **332**, 1429–1433 (2011).
- Pankiv, S. *et al.* p62/SQSTM1 binds directly to Atg8/LC3 to facilitate degradation of ubiquitinated protein aggregates by autophagy. *J. Biol. Chem.* **282**, 24131–24145 (2007).
- Bilmen, J. G., Khan, S. Z., Javed, M. H. & Michelangeli, F. Inhibition of the SERCA Ca²⁺ pumps by curcumin. Curcumin putatively stabilizes the interaction between the nucleotide-binding and phosphorylation domains in the absence of ATP. *Eur. J. Biochem.* **268**, 6318–6327 (2001).
- Chen, F. W., Li, C. & Ioannou, Y. A. Cyclodextrin induces calcium-dependent lysosomal exocytosis. *PLoS ONE* **5**, e15054 (2010).
- Trick, M. *et al.* Niemann-Pick type C1 patient-specific induced pluripotent stem cells display disease specific hallmarks. *Orphanet J. Rare Dis.* **8**, 144 (2013).
- Maetzel, D. *et al.* Genetic and chemical correction of cholesterol accumulation and impaired autophagy in hepatic and neural cells derived from Niemann-Pick Type C patient-specific iPS cells. *Stem Cell Rep.* **2**, 866–880 (2014).
- Yu, D. *et al.* Niemann-Pick disease type C: induced pluripotent stem cell-derived neuronal cells for modeling neural disease and evaluating drug efficacy. *J. Biomol. Screen.* **19**, 1164–1173 (2014).
- Liscum, L. & Faust, J. R. Low density lipoprotein (LDL)-mediated suppression of cholesterol synthesis and LDL uptake is defective in Niemann-Pick type C fibroblasts. *J. Biol. Chem.* **262**, 17002–17008 (1987).
- Griffin, L. D., Gong, W., Verot, L. & Mellon, S. H. Niemann-Pick type C disease involves disrupted neurosteroidogenesis and responds to allopregnanolone. *Nat. Med.* **10**, 704–711 (2004).
- Meske, V., Erz, J., Priesnitz, T. & Ohm, T. G. The autophagic defect in Niemann-Pick disease type C neurons differs from somatic cells and reduces neuronal viability. *Neurobiol. Dis.* **64**, 88–97 (2014).
- Liao, G. *et al.* Cholesterol accumulation is associated with lysosomal dysfunction and autophagic stress in *Npc1*^{−/−} mouse brain. *Am. J. Pathol.* **171**, 962–975 (2007).

35. Panyam, J. & Labhasetwar, V. Biodegradable nanoparticles for drug and gene delivery to cells and tissue. *Adv. Drug Deliv. Rev.* **55**, 329–347 (2003).
36. Aebischer, P. & Ridet, J. Recombinant proteins for neurodegenerative diseases: the delivery issue. *Trends Neurosci.* **24**, 533–540 (2001).
37. Loftus, S. K. *et al.* Murine model of Niemann-Pick C disease: mutation in a cholesterol homeostasis gene. *Science* **277**, 232–235 (1997).
38. Takahashi, K. *et al.* Induction of pluripotent stem cells from adult human fibroblasts by defined factors. *Cell* **131**, 861–872 (2007).
39. Billich, A. & Ettmayer, P. Fluorescence-based assay of sphingosine kinases. *Anal. Biochem.* **324**, 114–119 (2004).
40. Miyoshi, H., Blomer, U., Takahashi, M., Gage, F. H. & Verma, I. M. Development of a self-inactivating lentivirus vector. *J. Virol.* **72**, 8150–8157 (1998).
41. Kim, T. K. & Burgess, D. J. Pharmacokinetic characterization of 14C-vascular endothelial growth factor controlled release microspheres using a rat model. *J. Pharm. Pharmacol.* **54**, 897–905 (2002).
42. Okita, K., Ichisaka, T. & Yamanaka, S. Generation of germline-competent induced pluripotent stem cells. *Nature* **448**, 313–317 (2007).
43. Okabe, M. *et al.* Definitive proof for direct reprogramming of hematopoietic cells to pluripotency. *Blood* **114**, 1764–1767 (2009).
44. Okada, Y. *et al.* Spatiotemporal recapitulation of central nervous system development by murine embryonic stem cell-derived neural stem/progenitor cells. *Stem Cells* **26**, 3086–3098 (2008).
45. Imaizumi, Y. *et al.* Mitochondrial dysfunction associated with increased oxidative stress and alpha-synuclein accumulation in PARK2 iPSC-derived neurons and postmortem brain tissue. *Mol. Brain* **5**, 35 (2012).

Acknowledgements

We thank Victor A. DeAngelis for help with UPLC analysis. We are grateful to Hyun Ok Kim and Tomoyuki Yamaguchi for kindly providing reagents. This work was supported by the Bio & Medical Technology Development Program (2011-0019356,

2012M3A9C6050107, 2012M3A9C6049913) of the National Research Foundation (NRF) of Korea funded by the Ministry of Science, ICT & Future Planning, Republic of Korea. This study was also supported by a grant of the Korea Healthcare Technology R&D Project, Ministry for Health & Welfare, Republic of Korea (A120367).

Author contributions

H.L., J.K.L., M.H.P., Y.R.H., H.K., Y.O., M.O., E.-J.S., J.-H.P., J.-H.B., N.O., X.H. and H.K.J. performed the experiments and analysed the data. J.-S.B. and H.K.J. designed the study and H.L., J.K.L. and J.-S.B. wrote the paper. E.H.S., J.-S.B. and H.K.J. interpreted the data and reviewed the paper. H.H.M. generated and provided VEGF^{flb} mice. All authors discussed results and commented on the manuscript.

Additional information

Supplementary Information accompanies this paper at <http://www.nature.com/naturecommunications>

Competing financial interests: The authors declare no competing financial interest.

Reprints and permission information is available online at <http://npg.nature.com/reprintsandpermissions/>

How to cite this article: Lee, H. *et al.* Pathological roles of the VEGF/SphK pathway in Niemann–Pick type C neurons. *Nat. Commun.* **5**:5514 doi: 10.1038/ncomms6514 (2014).



This work is licensed under a Creative Commons Attribution 4.0 International License. The images or other third party material in this article are included in the article's Creative Commons license, unless indicated otherwise in the credit line; if the material is not included under the Creative Commons license, users will need to obtain permission from the license holder to reproduce the material. To view a copy of this license, visit <http://creativecommons.org/licenses/by/4.0/>

Correspondence

To the editor:

The *BRAF*-V600E mutation in circulating cell-free DNA is a promising biomarker of high-risk adult Langerhans cell histiocytosis

We read with great interest the recent review article on Langerhans cell histiocytosis (LCH) by Delprat and Aricò.¹ As they mentioned, LCH is a rare disorder characterized by local accumulation of dysplastic Langerhans cells and a wide range of organ involvement. Although the precise pathophysiology remains unknown, recent findings suggest that LCH is likely to be a clonally expanding myeloid neoplasm. One of the strongest lines of evidence is a report by Badalian-Very et al that the oncogenic *BRAF*-V600E mutation was detected in LCH lesions from a majority of patients.² Furthermore, Berres et al found that patients with active, high-risk LCH carried the *BRAF*-V600E mutation in circulating CD11c⁺/CD14⁺ cell fractions as well as in bone marrow CD34⁺ progenitor cells.³ In patients with various solid tumors, circulating cell-free DNA (cfDNA) in peripheral blood contains cancer-derived genomic DNA and has been used in a noninvasive diagnostic procedure, the so-called "liquid biopsy." In a recent report, *BRAF*-V600E was detected successfully in cfDNA from patients with colorectal cancer, with 100% sensitivity and specificity.⁴ LCH can involve organs and tissues not readily accessible for biopsy, and the specimens are sometimes not available for genetic analyses after pathologic procedures. Thus, we evaluated the *BRAF* mutation in cfDNA as a potential biomarker of LCH using an allele-specific quantitative polymerase chain reaction (ASQ-PCR).

We cloned normal and mutant *BRAF* alleles that included exon 15 and its neighboring sequences into pCR2.1 to prepare a standard curve. cfDNA was prepared from the plasma of adult LCH patients by using the QIAamp DNA Blood Mini Kit (Qiagen) and was subjected to genotyping for the *BRAF* alleles by ASQ-PCR that was specifically designed to detect *BRAF*-V600E by using a 3'-phosphate-modified oligonucleotide blocker, according to Thierry et al.⁴ Each assay reaction was performed in triplicate. The mutant *BRAF* load was estimated from the standard curve in each assay and was expressed as the mean percentage of mutant alleles relative to the total number of alleles by using the StepOnePlus Real-Time PCR System (Life Technologies).

Plasma cfDNA was prepared from 8 adult patients with LCH (listed in Table 1) as well as 8 normal participants. DNA from lesion tissues was not available for all patients. The mean quantity of cfDNA recovered from patients with LCH vs normal participants was 316.5 pg/mL (median, 290.4 pg/mL) vs 92.0 pg/mL (median,

91.8 pg/mL). Three high-risk patients with active multiple lesions were positive for *BRAF*-V600E but 8 normal participants were not. In these patients, the mean ratio of mutant *BRAF* alleles to total alleles was 3.25% (median, 2.59%). Immunohistochemical analyses that used a *BRAF*-V600E-specific antibody (Spring Bioscience) in biopsy specimens from 2 patients revealed that patient 3 (unique patient number 3 [UPN 3]) was positive for *BRAF*-V600E but UPN 7 was negative, which may be explained by the lower sensitivity of the detection method and/or the possibility that some but not all lesions are positive for *BRAF*-V600E in patients with multisystem LCH. Next, we compared the sensitivity of ASQ-PCR for *BRAF*-V600E between cfDNA and cellular DNA in the same blood sample. Naturally, much more DNA was recovered from mononuclear cells than from the same blood volume of plasma, but the ratio of mutant to total alleles was more than 10-fold higher in the cfDNA, suggesting that LCH-derived genomes are significantly enriched in cfDNA compared with cellular DNA and that cfDNA is adequate for liquid biopsies in LCH with *BRAF*-V600E.

Next, in UPN 7, we observed the mutant *BRAF* load during the course of initial chemotherapy. The ratio of mutant to total alleles was estimated as 1.00% prior to chemotherapy and was unmeasurable after chemotherapy. These data were compatible with the improved findings of computed tomography and positron emission tomography performed at the same time. Based on these results, ASQ-PCR for *BRAF*-V600E in cfDNA may contribute to planning risk-based treatment as well as monitoring treatment efficacy in LCH, especially in a group with active, high-risk LCH. Several *BRAF*-targeted inhibitors have been approved or are in clinical trials for various cancers with *BRAF* mutations, and one of those inhibitors, vemurafenib, is also active against LCH with *BRAF*-V600E.⁵

Despite an obviously very small cohort, we demonstrated the feasibility of *BRAF*-V600E in cfDNA as a biomarker of active, high-risk LCH. The utility of *BRAF*-V600E in cfDNA should be validated in a larger cohort of LCH patients.

Masayuki Kobayashi

Division of Molecular Therapy, Advanced Clinical Research Center,
Institute of Medical Science,
The University of Tokyo,
Tokyo, Japan

Table 1. Characteristics of patients with adult LCH

UPN	Age, years	Gender	Organ involvement	Risk	Activity	Treatment	<i>BRAF</i> -V600E immunohistostaining	<i>BRAF</i> -V600E (%)*
1	56	F	Multi	High	Inactive	Completed	N/A	0
2	38	F	Single	High	Inactive	Completed	N/A	0
3	65	F	Multi	High	Active	Interrupted	Positive	2.59 ± 0.21
4	48	M	Single	High	Inactive	During	N/A	0
5	41	F	Single	High	Inactive	During	N/A	0
6	28	M	Multi	High	Inactive	During	N/A	0
7	29	M	Multi	High	Active	Not started	Negative	1.00 ± 0.28
8	47	F	Multi	High	Active	Interrupted	N/A	6.16 ± 0.33

F, female; M, male; N/A, not available; UPN, unique patient number.

*Mean ± standard error.

Arinobu Tojo

Division of Molecular Therapy, Advanced Clinical Research Center,
Institute of Medical Science,
The University of Tokyo,
Tokyo, Japan

Acknowledgments: The authors thank Safia El Messaoudi and Alain R. Thierry (Institut de Recherche en Cancérologie de Montpellier, Montpellier, France) for technical advice in ASQ-PCR. We also appreciate Masanori Ohta for immunohistochemical analysis and the medical staff in the Department of Hematology/Oncology, Research Hospital, Institute of Medical Science, The University of Tokyo, for collecting samples from patients.

This work was supported by grants from the Japan LCH Study Group.

Contribution: M.K. designed and performed the experiment, analyzed data, and wrote the paper; and A.T. designed and supervised the experiment.

Conflict-of-interest disclosure: The authors declare no competing financial interests.

Correspondence: Masayuki Kobayashi, Division of Molecular Therapy, Advanced Clinical Research Center, Institute of Medical Science, The University

of Tokyo, 4-6-1 Shirokanedai, Minato-ku, Tokyo 108-8639, Japan;
e-mail: masa-k@ims.u-tokyo.ac.jp.

References

1. Delprat C, Aricò M. Blood spotlight on Langerhans cell histiocytosis. *Blood*. 2014; 124(6):867-872.
2. Badalian-Very G, Vergilio JA, Degar BA, et al. Recurrent BRAF mutations in Langerhans cell histiocytosis. *Blood*. 2010;116(11):1919-1923.
3. Berres ML, Lim KP, Peters T, et al. BRAF-V600E expression in precursor versus differentiated dendritic cells defines clinically distinct LCH risk groups. *J Exp Med*. 2014;211(4):669-683.
4. Thierry AR, Moulere F, El Messaoudi S, et al. Clinical validation of the detection of KRAS and BRAF mutations from circulating tumor DNA. *Nat Med*. 2014;20(4): 430-435.
5. Haroche J, Cohen-Aubart F, Emile JF, et al. Dramatic efficacy of vemurafenib in both multisystemic and refractory Erdheim-Chester disease and Langerhans cell histiocytosis harboring the BRAF V600E mutation. *Blood*. 2013;121(9): 1495-1500.

© 2014 by The American Society of Hematology

To the editor:**Calreticulin mutation does not modify the IPSET score for predicting the risk of thrombosis among 1150 patients with essential thrombocythemia**

An international prognostic score for the risk of thrombosis (IPSET-thrombosis) in essential thrombocythemia (ET) was developed.¹ Risk factors included the following: age >60 years (1 point), cardiovascular (CV) risk factors (1 point), previous thrombosis (2 points), and the presence of *JAK2V617F* mutation (2 points). Low-, intermediate-, and high-risk categories were identified by scores 0 to 1, 2, and ≥3, respectively. Mutations in the exon 9 of calreticulin (*CALR*) gene were recently identified in a large proportion of patients with *JAK2V617F*-negative ET and associated with a

reduced thrombotic risk as compared with *JAK2V617F*-positive patients.²⁻⁵ However, the utility of incorporating *CALR* mutation status into current risk stratification for thrombosis in ET is not yet tested. Answering this question was the purpose of the present study.

Under the auspices of the Associazione Italiana per la Ricerca sul Cancro Gruppo Italiano Malattie Mieloproliferative, 4 Italian centers convened to create a database of 1150 patients previously diagnosed with and treated for ET. The study was approved by each Institutional Review Board. Patients' eligibility criteria included diagnosis

Table 1. Patients' characteristics at diagnosis

	Total	<i>CALR</i> + (A)	<i>JAK2V617F</i> + (B)	<i>MPLW515</i> + (C)	<i>CALR</i> , <i>JAK2</i> , <i>MPL</i> wild type (D)	<i>P</i> A vs B	<i>P</i> A vs C	<i>P</i> A vs D
Number of patients, (%)	1150*	164 (14)	736 (64)	44 (4)	198 (17)			
Gender M/F, n (%)	403/739 (35/65)	84/80 (51/49)	266/470 (36/64)	13/31 (30/70)	40/158 (20/80)	<.0001	.010	<.0001
Age, years, median (5th-95th percentile)	57.6 (27-82)	53.5 (27-81)	60.8 (28-83)	59.7 (27-87)	47.8 (21-78)	.001	.396	.245
Hemoglobin, g/dL, median (5th-95th percentile)	14.1 (11.8-16.3)	13.7 (11.6-16.1)	14.5 (11.9-16.4)	13.4 (11.6-16.0)	13.6 (11.7-15.8)	<.0001	.681	.099
Hematocrit, %, median (5th-95th percentile)	43.0 (36.0-48.8)	42.1 (35.6-47.6)	43.7 (37.2-49.3)	41.8 (35.0-48.5)	41.0 (35.1-47.0)	.002	.880	.133
White blood cell count, ×10 ⁹ /L, median (5th-95th percentile)	8.7 (5.4-14.7)	7.8 (5.2-12.0)	9.0 (5.7-15.1)	7.9 (4.8-14.0)	8.4 (5.3-14.0)	<.0001	.725	.034
Platelet count, ×10 ⁹ /L, median (5th-95th percentile)	718 (486-1313)	842 (551-1769)	704 (490-1234)	834 (544-1700)	647 (464-1318)	<.0001	.971	<.0001
CV risk factors, n (%)	568 (50)	71 (43)	386 (52)	27 (61)	84 (42)	.034	.033	.868
Smoke, n (%)	98 (9)	7 (4)	66 (9)	5 (11)	20 (10)	.046	.073	.035
Diabetes, n (%)	107 (9)	11 (7)	77 (10)	5 (11)	14 (7)	.143	.303	.892
Hypertension, n (%)	459 (40)	59 (36)	314 (43)	21	65	.116	.497	.175
Previous major thrombosis, n (%)	167 (15)	13 (8)	122 (17)	9 (20)	23 (12)	.005	.016	.243
IPSET score, n (%)						<.0001	<.0001	.124
Low risk, n (%)	263 (23)	110 (67)	0 (0)	17 (39)	136 (69)			
Intermediate risk, n (%)	316 (28)	48 (29)	206 (28)	16 (36)	46 (23)			
High risk, n (%)	563 (49)	6 (4)	530 (72)	11 (25)	16 (8)			

*Eight patients with double positivity for *JAK2V617F* and *MPLW515* were excluded from further analysis

Research Article

DNA Methylation Is Involved in the Expression of miR-142-3p in Fibroblasts and Induced Pluripotent Stem Cells

Siti Razila Abdul Razak,¹ Yukihiro Baba,¹ Hiromitsu Nakauchi,²
Makoto Otsu,² and Sumiko Watanabe¹

¹Division of Molecular and Developmental Biology, Institute of Medical Science, University of Tokyo, 4-6-1 Shirokanedai, Minato-ku, Tokyo 108-8639, Japan

²Division of Stem Cell Therapy, Center for Stem Cell Biology and Regenerative Medicine, Institute of Medical Science, University of Tokyo, 4-6-1 Shirokanedai, Minato-ku, Tokyo 108-8639, Japan

Correspondence should be addressed to Sumiko Watanabe; sumiko@ims.u-tokyo.ac.jp

Received 11 August 2014; Revised 4 November 2014; Accepted 14 November 2014; Published 2 December 2014

Academic Editor: Chia-Lin Wei

Copyright © 2014 Siti Razila Abdul Razak et al. This is an open access article distributed under the Creative Commons Attribution License, which permits unrestricted use, distribution, and reproduction in any medium, provided the original work is properly cited.

MicroRNAs are differentially expressed in cells and regulate multiple biological processes. We have been analyzing comprehensive expression patterns of microRNA in human and mouse embryonic stem and induced pluripotent stem cells. We determined microRNAs specifically expressed in these pluripotent stem cells, and miR-142-3p is one of such microRNAs. miR-142-3p is expressed at higher levels in induced pluripotent stem cells relative to fibroblasts in mice. Level of expression of miR142-3p decreased during embryoid body formation from induced pluripotent stem cells. Loss-of-function analyses of miR-142-3p suggested that miR-142-3p plays roles in the proliferation and differentiation of induced pluripotent stem cells. CpG motifs were found in the 5' genomic region of the *miR-142-3p*; they were highly methylated in fibroblasts, but not in undifferentiated induced pluripotent stem cells. Treating fibroblasts with 5-aza-2'-deoxycytidine increased the expression of miR-142-3p significantly and reduced methylation at the CpG sites, suggesting that the expression of miR-142-3p is suppressed by DNA methylation in fibroblasts. Luciferase analysis using various lengths of the 5' genomic region of miR142-3p indicated that CpGs in the proximal enhancer region may play roles in suppressing the expression of miR-142-3p in fibroblasts.

1. Introduction

The self-renewal and differentiation of pluripotent stem cells are regulated by various factors including growth factors, cytokines, intracellular signaling molecules, the extracellular matrix, and transcription factors. In addition, the roles of microRNAs (miRNAs) and epigenetic regulation such as DNA methylation and histone modification have received increasing attention in recent years [1]. The complex regulatory networks involving these mechanisms have been studied extensively in embryonic stem (ES) and induced pluripotent stem (iPS) cells and have revealed that the regulatory activity, in combination with transcription factors, is associated with pluripotency [2].

We previously assessed the expression pattern of miRNAs in human and mouse ES and iPS cells [3]. We found that

several miRNAs were highly expressed in undifferentiated iPS cells [3]. Among these, we focused on miRNA- (miR-) 142-3p in the current study. miR-142 was first identified in hematopoietic cells [4], where it plays various roles in differentiation and functions during hemopoiesis [5–7]. miR-142 is highly conserved among vertebrates [8] and has been implicated in cardiac cell fate determination [9], osteoblast differentiation [10], and vascular development [11]. In cancer, *miR-142-3p* was identified at the breakpoint of a *MYC* translocation in B-cell leukemia [12] and was mutated in 20% of diffuse large B-cell lymphomas [13]. It is also critically involved in T-cell leukemogenesis [14] and the migration of hepatocellular carcinoma cells [15].

miRNAs are transcribed by RNA polymerase II [16], which involves various transcription factors. In hematopoietic cells, specifically, Spi1, Cebpb, Runx1, and LMO2 have

all been reported to regulate miR-142 expression [17, 18]. However, these transcription factors are mostly hematopoietic cell-specific, suggesting that the expression of miR-142 in undifferentiated iPS cells involves regulation of other factors. In this study, we examined the roles of miR-142-3p in iPS cells and found that miR-142-3p might be involved in the proliferation of iPS cells and in maintaining their immaturity. Furthermore, miR-142-3p might also play roles in the mesodermal differentiation of iPS cells. Our data suggest roles for the methylation of CpG motifs in the 5' genomic region of miR-142-3p in suppressing its expression in fibroblasts. Luciferase analysis of the isolated genomic region of miR-142-3p supports the idea that the expression of miR-142-3p in cells including fibroblasts and iPS is regulated, at least partially, by DNA methylation.

2. Materials and Methods

2.1. Cell Lines, 5-Aza-2'-deoxycytidine (5-Aza-dC) Treatment, and Transfection. 3T3 cells were cultured in the DMEM (Nacalai Tesque) supplemented with 10% fetal bovine serum (GIBCO) and 0.5% penicillin/streptomycin (Nacalai Tesque). Preparation and culture of mouse embryonic fibroblast (MEF) and tail-tip fibroblasts (TTF) are described previously [3]. ICR mice were purchased from local dealers, and all experiments with animals were approved by the Animal Care Committee of the Institute of Medical Science at the University of Tokyo. Mouse iPS cell line, SP-iPS, was from B6 mouse MEF with infection of 4 factors (Sox2, Oct3/4, Klf4, and c-myc) by using retrovirus [19]. Culture of the iPS cells and formation of embryoid body (EB) is described previously [3]. For treatment of 5-aza-dC, cells were treated with final concentration of 5 or 10 μ M 5-aza-dC (SIGMA) or dimethyl sulfoxide (DMSO) for control samples 6 hours after the cells were plated, and cells were cultured for 3 days before analysis unless otherwise noted. For plasmid transfection, 3T3 cells were plated in a 24-well culture plate 1 day before transfection. Transfection of luciferase plasmid was done by using Gene Juice Transfection Reagent (Novagen). Briefly, Gene Juice Reagent (1.5 μ L), plasmid (0.25 μ g in 0.25 μ L for each plasmid), and Opti-MEM (Gibco-Life Technologies) were mixed and added to 3T3 cells. For plasmid transfection to iPS, electroporation was employed. iPS cells were dissociated into single cells by 0.05% trypsin-EDTA, washed with PBS, and resuspended in Opti-MEM. For each transfection, 1×10^6 cells/30 μ L were gently mixed with 15 μ g of plasmid and placed in 2 mm gap electroporation cuvette (Nepa Gene Co., Ltd.). The cells were electroporated for two times at 175 V, 2 ms at 50 ms interval (CUY21 EDIT, Nepa Gene Co., Ltd.). Immediately after electroporation, 1 mL of iPS culture medium was gently added to the cuvette, and cells were transferred and cultured on feeder cells in iPS medium. On the following day, the cells were dissociated and stained with SSEA-1 marker. Subsequently, the GFP + SSEA-1 + double positive cells from study or control group were sorted by FACS (MoFlo, DakoCytomation) and used for cell proliferation and colony formation assay.

2.2. RNA Extraction and Real-Time PCR for Quantification of miRNAs and mRNA. Total RNA was extracted using the Sepasol (Nacalai Tesque), and level of mature miRNAs was detected using TaqMan MicroRNA systems (Applied Biosystems) using primer specific for each mature miRNA supplied by Applied Biosystems using Light Cyclers 1.5 (ROCHE). Briefly, a total of 500 ng RNA were reverse-transcribed with Taqman Reverse-Transcription PCR Kit with specific primer for miR-142-3p. Then, cDNA was mixed with TaqMan Universal Master Mix (Applied Biosystems) and was subjected for real-time PCR. Ct value was analyzed with SDS 2.4 and RQmanager 1.2.1 and quantitated using $2^{-\Delta\Delta C_t}$ method (Livak, 2001). All data were normalized to endogenous control, the U6 snRNA. Sequences of the primers are T/brachyury 5'-cacaccactgacgcacacggt-3', 5'-atgaggaggccttggggcgt-3', Gata4 5'-agccggtgggtgatccgaag-3', 5'-agaaatcgtgcgggaggcg-3', Fgf5 5'-gcagtcgagcaaccggaact-3', and 5'-ggacttctgcgaggctgca-3'. For quantification of mRNA, total RNA (1 μ g) from each sample was used to generate cDNA using ReverTra Ace qRT-PCR RT Kit (Toyobo). Then, cDNA was mixed with Sybr Green Master Mix (ROCHE) and was subjected for real-time PCR using Light Cyclers 1.5 (ROCHE). Expression levels of mRNA were compared to known standard samples and normalized to GAPDH.

2.3. Isolation and Bisulfite Treatment of Genomic DNA. Genomic DNA was isolated from $\sim 5 \times 10^6$ cells using the QIAamp DNA Mini and Blood Mini kit (Qiagen). Genomic DNA (1 μ g) was subjected for bisulfite conversion using EpiTect Bisulfite (Qiagen). The converted DNA was further subjected to PCR for A-tailing procedure with HotStarTaq DNA Polymerase (Qiagen). Regions covering up to 700 bp upstream of the miR-142 seed sequence were amplified and were cloned into pGEM-T Easy Vector (Invitrogen). All positive clones were sequence and methylation results obtained were analyzed by Quantification Tool for Methylation Analysis (QUMA, <http://quma.cdb.riken.jp>) which was used for detection of CpG island methylation [20].

2.3.1. DNA Construction. Plasmids containing antisense sequences of mature miR-142-3p or miR-17 expression plasmid were constructed as follows: double strand DNA, which encode antisense of mature miR-142-3p or miR-17, was inserted downstream of U6 promoter using BamHI and EcoRI sites of pMX retrovirus vector containing EGFP after 5' LTR (Figure 1(b)). Expression plasmids for mouse Oct4, Sox2, Klf, and Myc were purchased from AddGene.

2.3.2. Cell Sorting, Cell Staining with Alkaline Phosphatase (ALP), and Immunostaining. Cells' sorting was done using a MoFlo (DakoCytomation). ALP staining was done using BCIP-NBT solution kit for alkaline phosphatase stain (Nacalai Tesque) according to the manufacturer's instructions. Immunostaining was done using antibody anti-Ki67 proliferation antigen (BD Biosciences), and the primary antibody was visualized using appropriate secondary antibody conjugated with Alexa 488 (Molecular Probes).

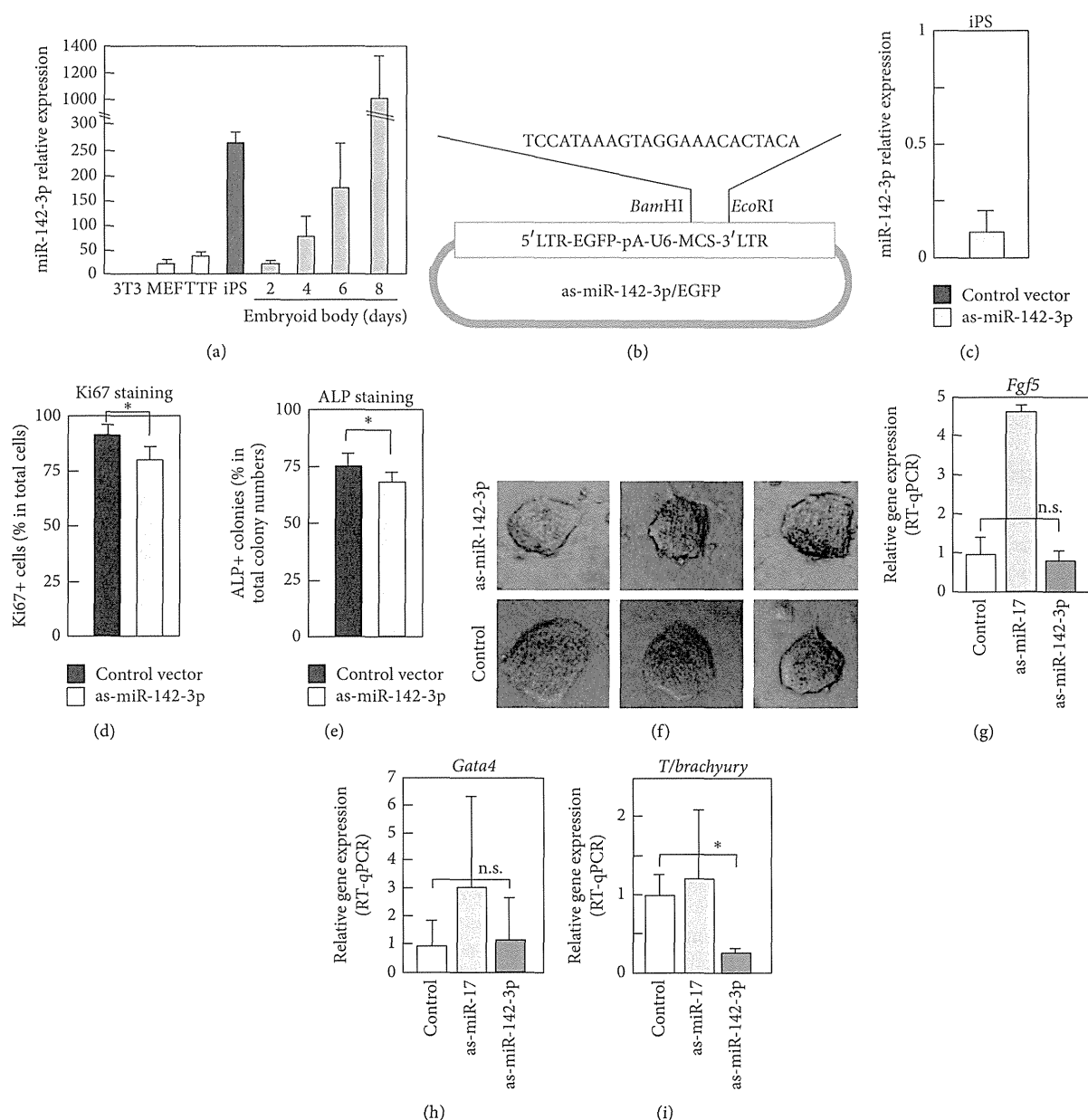


FIGURE 1: Differential expression level of miR-142-3p in fibroblasts and iPS. (a) Expression of miR-142-3p was examined by RT-qPCR in various cells. Total RNA was extracted from indicated cells, and RT-qPCR was done using TaqMan MicroRNA systems. U6 shRNA was used as a control. Experiments were done three times using independently prepared cells, and average values with standard deviation are shown. (b) Schematic representation of antisense- (as-) miR-142-3p and EGFP expression plasmid. LTR was used to drive EGFP, and U6 promoter was used to drive as-miR-142-3p. (c) Effect of overexpressed as-miR-142-3p for expression level of endogenous miR-142-3p in iPS cells. as-miR-142-3p/EGFP or control vector was transfected into iPS, and, after 24 hours, level of miR-142-3p in iPS was examined by RT-qPCR. Data were expressed as relative expression level of miR-142-3p in as-miR-142-3p/EGFP expressing cells to that in control vector expressing cells. Experiments were performed three times, and average values with standard deviation are shown. (d, e, and f) Effects of expression of as-miR-142-3p for proliferation and alkaline phosphatase (ALP) expression of iPS. as-miR-142-3p/EGFP plasmid was transfected into undifferentiated iPS, and EGFP positive cells were purified by a cell sorter. Then EGFP positive cells were cultured for 2 days for Ki67 immunostaining and for 5 days for ALP assay. Immunostaining with anti-Ki67 antibody or ALP staining was done, and positive cells were counted under a microscope. Experiments were performed three times, and average values with standard deviation are shown. In (f), morphology of representative colonies of as-miR-142-3p or control vector transfected iPS is shown. (g–i) Expression of lineage marker genes in embryoid body (EB). iPS cells were transfected with as-miR-142-3p/EGFP or as-miR-17/EGFP as a control, purified according to their expression of EGFP, and then subjected to an EB formation. After 6 days of culturing in EB formation condition, the differentiation of cells into the ectodermal (g), endodermal (h), and mesodermal (i) lineages was assessed using RT-qPCR with primers against *Fgf5*, *Gata4*, and *T brachyury*, respectively. *P* value, * < 0.05 and n.s. > 0.05, was calculated by Student's *t*-test.

2.3.3. Luciferase Analysis. 3T3 cells were plated in a 24-well culture plate 1 day before transfection and transfected with luciferase plasmid (0.25 μ g) by using Gene Juice Transfection Reagent (Novagen). Six hours after transfection, cells were treated with final concentration of 10 μ M of 5-azacytidine and were cultured for 3 days. Cells were harvested using Cell Culture Lysis Reagent 5X (Promega). Luciferase activity toward a luciferase assay substrate (Promega) was measured with a luminometer (Lumat LB9507, Berthold Technologies).

3. Results

3.1. Characterization of miR-142-3p Expression in iPS Cells, Embryoid Bodies, and Fibroblasts. We previously characterized the expression pattern of miRNAs in mouse and human iPS and ES cells using miRNA arrays and found that miR-142-3p, but not miR-142-5p, was expressed at high levels in iPS cells (see Supplementary Figure 1 available online at <http://dx.doi.org/10.1155/2014/101349>) [3]. We first confirmed the expression pattern of miR-142-3p using quantitative reverse transcription-polymerase chain reaction (qRT-PCR). miR-142-3p was expressed at a high level in undifferentiated iPS cells, whereas fibroblasts such as 3T3, mouse embryonic fibroblasts (MEFs), and tail-tip fibroblasts (TTF) expressed only very low levels (Figure 1(a)). When iPS cells were differentiated by formation of embryoid bodies (EBs), the expression of miR-142-3p fell to very low levels on day 2 but then increased on the following days (Figure 1(a)).

3.1.1. Functional Analyses of miR-142-3p in iPS Cell Physiology. We next constructed an expression plasmid encoding antisense miR-142-3p (as-miR-142-3p) and enhanced green fluorescent protein (EGFP; Figure 1(b)). A plasmid without insertion of antisense miR-142-3p was used as a control for all experiments. The effect of expressing as-miR-142-3p on endogenous miR-142-3p was then examined and confirmed in mouse iPS cells (Figure 1(c)). Specifically, as-miR-142-3p/EGFP was transfected into undifferentiated iPS to analyze the role of miR-142-3p in the proliferation and maintenance of immaturity in iPS cells. Twenty-four hours after transfection, EGFP-positive cells were purified using a cell sorter and cultured for 3 days. Cell proliferation was then assessed by immunostaining for Ki67, a proliferative marker (Figure 1(d)). The population of Ki67-positive cells was slightly, but significantly, lower in as-miR-142-3p-expressing iPS cells (Figure 1(d)). We then counted the number of alkaline phosphatase- (ALP-) positive iPS colonies, and significantly fewer ALP-positive cells were found within the as-miR-142-3p-expressing iPS colonies (Figure 1(e)). Morphology of colonies of iPS cell was indistinguishable between control and as-miR-142-3p expressing samples (Figure 1(f)).

We then analyzed the roles of miRNA-142-3p on the ability of iPS cells to differentiate. iPS cells were transfected with as-miR-142-3p/EGFP, purified according to their expression of EGFP, and then subjected to an EB formation assay. An expression plasmid containing antisense sequence against miR-17, which is expressed at very high levels in undifferentiated iPS cells [3, 21], was used as a control.

After 6 days, the differentiation of cells into the ectodermal, endodermal, and mesodermal lineages was assessed using real-time quantitative PCR (qPCR) with primers against *Fgf5*, *Gata4*, and *T brachyury*, respectively (Figures 1(g), 1(h), and 1(i)). Data revealed that as-miR-142-3p, but not as-miR-17, suppressed the expression of *T brachyury*, which is expressed specifically in cells of the mesodermal lineage [22] (Figure 1(i)). The expression of as-miR-142-3p did not affect the expression of *Fgf5* or *Gata4*, although as-miR-17 enhanced expression of *Fgf5*, as expected (Figures 1(g) and 1(h)).

3.2. 5-Aza-2'-deoxycytidine Treatment Upregulates miR-142-3p in Fibroblasts. To assess the transcriptional regulation of miR-142-3p expression, we examined its 5' genomic sequence and identified 25 CpG motifs in a region covering ~1000 base pairs (bp) upstream of the miR-142-5p core sequence (Supplementary Figure 2). We hypothesized that miR-142-3p expression is regulated epigenetically by DNA methylation in iPS cells and fibroblasts. MEFs and 3T3 cells were treated for 3 days with 5 or 10 μ M of 5-aza-2'-deoxycytidine (5-aza-dC), a DNA methyltransferase inhibitor (Dnmt), and the levels of miR-142-3p were assessed using real-time qPCR. The expression of miR-142-3p was upregulated by 5-aza-dC treatment (Figures 2(a) and 2(b)). In contrast, the levels of miR-17 were rather reduced but not significantly by 5-aza-dC (Figure 2(c)), whereas the expression of neither miR-142-3p nor miR-17 was changed significantly by 5-aza-dC in undifferentiated iPS cells (Figures 2(d) and 2(e)). We also examined the effects of 5-aza-dC on miR-142-3p in EBs and found that 10 μ M 5-aza-dC rather suppressed the expression (Figure 2(f)). We also examined the effects of 5-aza-dC for miR-142-3p expression in thymocytes. Levels of miR-142-3p were upregulated slightly by 10 μ M of 5-aza-dC, but to a much lesser extent than observed in fibroblasts (Figure 2(g)). Taken together, these results suggest that miR-142-3p is suppressed by DNA methylation in fibroblasts but that the downregulation of miR-142-3p during EB formation might be regulated by a different mechanism.

3.3. Proximal CpGs in the miR-142-3p Genomic Region Regulate Transcriptional Activity. We next performed promoter analyses of different fragments of the 5' upstream region of miR-142-3p using luciferase assays. Previous reports indicated that transiently transfected plasmids could be CpG-methylated in the cells *de novo* [23, 24]. Luciferase constructs were transfected into 3T3 cells, which were cultured in the presence or absence of 5-aza-dC for 3 days. Luciferase assays were then performed. In the absence of 5-aza-dC, the -274, -540, and -860 Luc constructs showed significant luciferase activity, which increased gradually when longer promoters were used (Figure 3(a)). In contrast, -1130 Luc had very low luciferase activity, suggesting the presence of a region between -860 and -1130 nucleotides (nt) that inhibited luciferase activity. When cells were cultured in the presence of 5-aza-dC, the luciferase activity of -274 Luc was upregulated significantly (Figure 3(a)). Since there are six CpGs in the region covering -274 to ATG, we speculated that

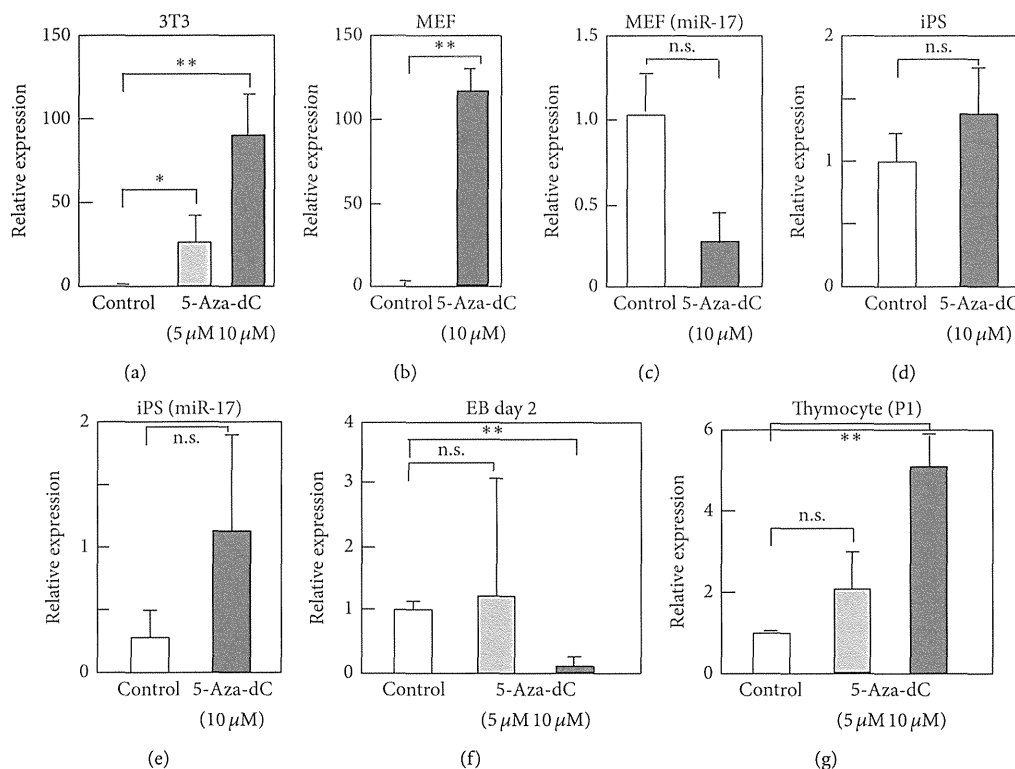


FIGURE 2: 5-Aza-2'-deoxycytidine (5-aza-dC) treatment upregulates miR-142-3p in fibroblasts. (a–g) 3T3 (a), MEF (b, c), iPS (d, e), embryoid body (EB) formed from mouse iPS (f), or mouse thymocytes (g) were treated with 5-aza-dC at indicated final concentration (5 or 10 μ M). Cells were cultured for 3 days in the presence of 5-aza-dC, except for EB, which was treated with 5-aza-dC for two days. Control cells were treated with DMSO. Then, cells were harvested, and total RNA was extracted. Level of miR-142-3p or miR-17 was examined by RT-qPCR. Value of U6 was used as a control. Values are expressed as relative to those of control samples of each cell type and are average of 3 or 4 times experiments with standard deviation. *P* value, ** < 0.01, 0.01 < * < 0.05, and n.s. > 0.05, was calculated by Student's *t*-test.

the methylation status of the proximal six CpGs might play roles in the upregulation of luciferase activity.

3.4. CpG Methylation in the 5' Genomic Region of miR-142-3p. To further elucidate the role of CpG sites and DNA methylation in regulating the expression of miR-142-3p, we analyzed the methylation status of the CpG sites identified in the region up to 700 bp upstream of the pre-miR-142-5p core region (Supplementary Figure 2) using bisulfite conversion. Analyses performed in 3T3 cells and MEFs revealed that the CpG sites were hypermethylated (Figures 3(b) and 3(c)). In contrast, those in undifferentiated iPS cells were hypomethylated (Figure 3(d)). We then analyzed the effects of 5-aza-dC on the methylation status in 3T3 cells and MEFs. Treatment with 5-aza-dC lowered methylation levels significantly, particularly at the proximal eight CpGs (Figures 3(e) and 3(f)). CpGs were also hypomethylated in day 5 EBs (Figure 3(g)), even though the expression of miR-142-3p was much lower than in undifferentiated iPS cells (Figure 1(a)).

3.5. Roles of Pluripotency-Related Transcription Factors in miR-142-3p Gene Activation. We next investigated the possible involvement of the pluripotency-associated transcription

factors Oct4, Sox2, Klf4, and c-Myc in the regulation of miR-142-3p transcription. The miR-142-3p promoter-luciferase construct (–540 Luc) was transfected into 3T3 cells with one of the four transcription factors, and luciferase assays were performed 3 days later. Luciferase activity was strongly upregulated by Klf4, whereas the other three transcription factors suppressed luciferase activity (Figure 3(h)). In addition, cotransfection with Klf4 and one of Oct4, Sox2, and c-Myc lowered luciferase activity compared with Klf4 alone (Figure 3(h)). We then analyzed the effects of overexpressing these transcription factors on the expression of endogenous miR-142-3p in 3T3 cells, but no effects were observed (Figure 3(i)).

4. Discussion

This study revealed that miR-142-3p is expressed in undifferentiated iPS cells, but not in fibroblasts, and DNA methylation might play a pivotal role in suppressing miR-142-3p expression in fibroblasts. Previous studies revealed that the transcription of miRNAs could be regulated by DNA methylation [25, 26]. miR-142-3p was reported to be upregulated in the human melanoma cell line WM1552C after treatment with

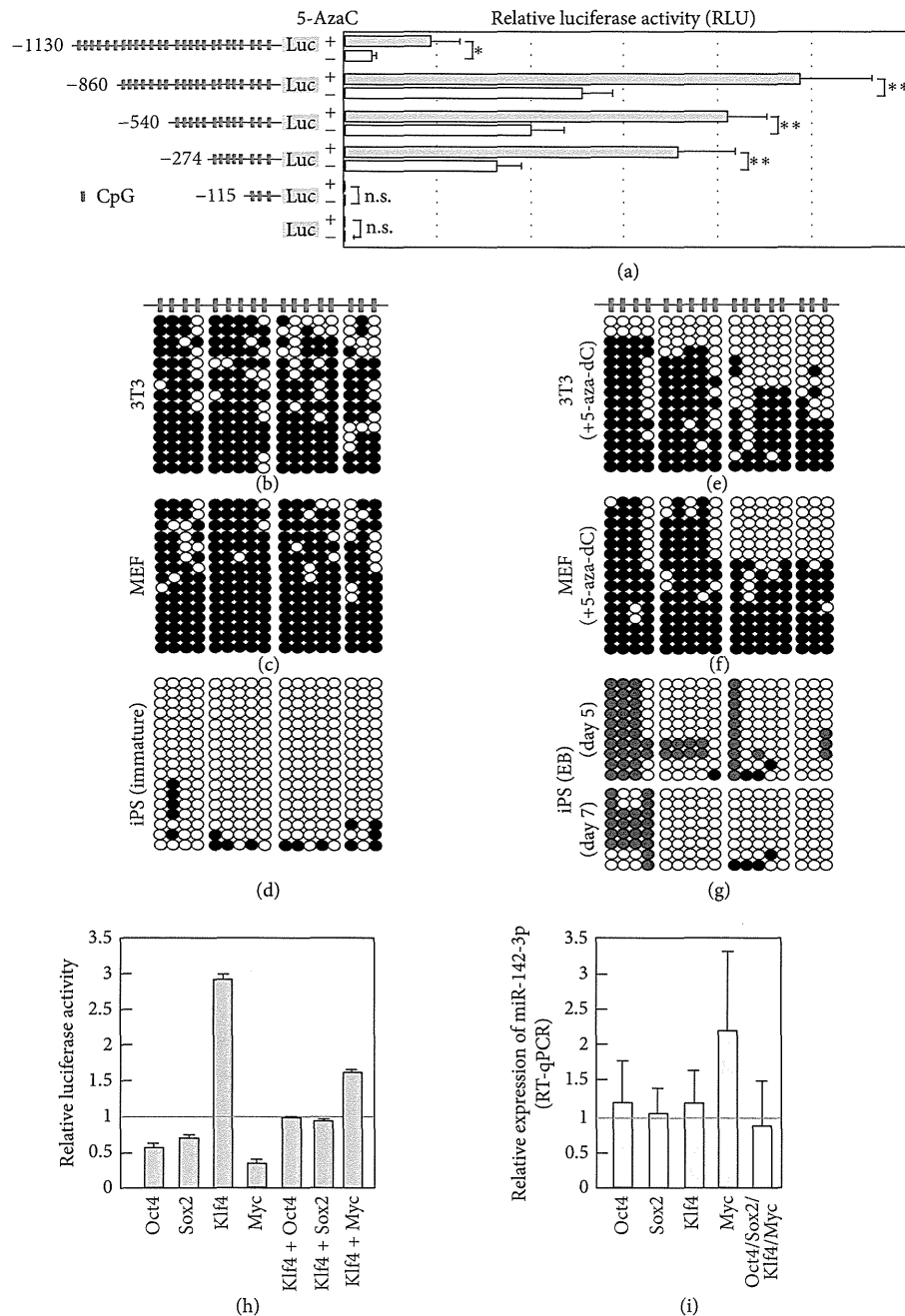


FIGURE 3: Expression of miR-142-3p was regulated by DNA methylation. (a) Left panel shows schematic representation of luciferase constructs. Luciferase analysis using plasmids containing indicated length fragments of the 5' upstream region of miR-142-3p-luciferase was done. Plasmid was transfected into 3T3 cells, and, after 6 hours, samples were treated with DMSO or 5-aza-dC (10 μ M) and cultured for additional 3 days. Then cells were harvested, and luciferase activities were examined. Values are average of 3 times independent experiments with standard deviation. *P* value, ** < 0.01 and n.s. > 0.05, was calculated by Student's *t*-test. (b–g) CpG methylation of 5' upstream region of miR-142-3p was examined by bisulfite conversions. Genomic DNAs extracted from 3T3, MEF in the presence or absence of 5-aza-dC, iPS, or EB prepared from iPS were subjected to bisulfite sequence. 5-Aza-dC was present in the culture medium of 3T3 or MEF 72 hours before harvesting cells for genomic DNA extraction (e, f). (h) 3T3 cells were transfected with expression plasmid of Oct4, Sox2, Klf4, or Myc with –540 Luc. For control sample, empty expression plasmid and –540 Luc were transfected. Cells were harvested after 3 days of culture, and luciferase analysis was conducted. (i) 3T3 cells were transfected with indicated expression plasmid, and, after 3 days, cells were harvested, and total RNA was extracted. Expression level of endogenous miR-142-3p was examined by RT-qPCR. (h, i) Values are relative to control vector transfected samples and average of 4 independent samples with SD.

5-aza-dC [27], suggesting that the expression of miR-142-3p was attenuated by DNA methylation not only in fibroblasts, but also in melanocyte lineage cells. In the current study, 5-aza-dC did not enhance the expression of miR-142-3p in mouse P1 thymocytes, supporting the hypothesis that DNA methylation is not a major mechanism that regulates the expression of miR-142-3p in hematopoietic cells.

The expression of miR-142-3p in hematopoietic cells is regulated by various transcription factors that also play important roles in hematopoiesis [17, 18]. The sequence of pre-miR-142 is highly conserved among vertebrates [8]. In addition, the expression of human miR-142 was recently reported to be regulated by the methylation of a CpG in its enhancer region in mesenchymal cells [8]. Although no similarity was found in the mouse and human upstream genomic regions (~2000 nt) of miR-142-3p, miR-142 expression is regulated by CpG methylation in both species.

Methylation changes occur predominantly at the end of reprogramming. The genomic region harboring pluripotency-associated genes including Nanog, Oct4, and Zfp42 is demethylated very late during reprogramming [28]. When 5-aza-dC is present during this period, an increased number of embryonic stem cell-like colonies are observed [29]. Furthermore, 5-aza-dC enhances the generation of iPS cells by inhibiting Dnmt1 activity [30]. The expression of miR-142-3p might be desilenced by the suppression of DNA demethylation and stimulated by other genes that play roles in the late phase of reprogramming. We observed that Klf4 upregulated luciferase activity but that Klf4 did not enhance the expression of endogenous miR-142-3p in 3T3 cells. Therefore, we hypothesize that a molecular environment related to reprogramming, which 3T3 cells lack, might be required for miR-142-3p expression. We identified several potential binding sites for c-Myc and Sox2 in the genomic region up to 1 kb from the miR-142 mature sequence using the Genomatix Software Suite (<http://www.genomatix.de/solutions/genomatix-software-suite.html>). Therefore, the combination of these transcription factors in a wider genomic region might cooperate for the full induction of miR-142-3p expression.

TGF- β R1 and TGF- β R2 were both predicted to be targets of miR-142-3p [31], and TGF- β R1 was identified as a direct target in non-small-cell lung cancer [32]. TGF- β 1 is involved in the reprogramming process in which the inhibition of TGF- β signaling enhances the efficiency of reprogramming [33]. More recently, a report indicated that the miR-142-3p-mediated regulation of Wnt signaling could modulate the proliferation of mesenchymal progenitors [34]. The identification of miR-142-3p target genes in the TGF- β and Wnt signaling pathways further supports the hypothesis that miR-142-3p is involved in the regulation of iPS cell physiology.

5. Conclusions

miR-142-3p, which is highly expressed in iPS cells but not in fibroblasts, plays roles in the proliferation and differentiation of iPS cells. The expression of miR-142-3p is suppressed by DNA methylation of its CpG motifs in the 5' genomic region in fibroblasts.

Conflict of Interests

The authors declare that there is no conflict of interests regarding the publication of this paper.

Acknowledgments

The authors acknowledge Dr. Keiko Akagawa for technical assistance and Ms. Ying Sze Tsang for initiating this project. This work is supported by a grant-in-aid from the Ministry of Education, Culture, Sports, Science, and Technology of Japan.

References

- [1] G. Keller, "Embryonic stem cell differentiation: emergence of a new era in biology and medicine," *Genes & Development*, vol. 19, no. 10, pp. 1129–1155, 2005.
- [2] B. E. Bernstein, T. S. Mikkelsen, X. Xie et al., "A bivalent chromatin structure marks key developmental genes in embryonic stem cells," *Cell*, vol. 125, no. 2, pp. 315–326, 2006.
- [3] S. R. A. Razak, K. Ueno, N. Takayama et al., "Profiling of MicroRNA in human and mouse ES and iPS cells reveals overlapping but distinct MicroRNA expression patterns," *PLoS ONE*, vol. 8, no. 9, Article ID e73532, 2013.
- [4] C.-Z. Chen and H. F. Lodish, "MicroRNAs as regulators of mammalian hematopoiesis," *Seminars in Immunology*, vol. 17, no. 2, pp. 155–165, 2005.
- [5] Y. Sun, S. Varambally, C. A. Maher et al., "Targeting of microRNA-142-3p in dendritic cells regulates endotoxin-induced mortality," *Blood*, vol. 117, no. 23, pp. 6172–6183, 2011.
- [6] X. S. Wang, J. N. Gong, J. Yu et al., "MicroRNA-29a and microRNA-142-3p are regulators of myeloid differentiation and acute myeloid leukemia," *Blood*, vol. 119, no. 21, pp. 4992–5004, 2012.
- [7] R. Nimmo, A. Ciau-Uitz, C. Ruiz-Herguido et al., "MiR-142-3p controls the specification of definitive hemangioblasts during ontogeny," *Developmental Cell*, vol. 26, no. 3, pp. 237–249, 2013.
- [8] M. Skårn, T. Barøy, E. W. Stratford, and O. Myklebost, "Epigenetic regulation and functional characterization of microRNA-142 in mesenchymal cells," *PLoS ONE*, vol. 8, no. 11, Article ID e79231, 2013.
- [9] T. Nishiyama, R. Kaneda, T. Ono et al., "miR-142-3p is essential for hematopoiesis and affects cardiac cell fate in zebrafish," *Biochemical and Biophysical Research Communications*, vol. 425, no. 4, pp. 755–761, 2012.
- [10] W. Hu, Y. Ye, W. Zhang, J. Wang, A. Chen, and F. Guo, "MiR-142-3p promotes osteoblast differentiation by modulating Wnt signaling," *Molecular Medicine Reports*, vol. 7, no. 2, pp. 689–693, 2013.
- [11] M. K. Lalwani, M. Sharma, A. R. Singh et al., "Reverse genetics screen in Zebrafish identifies a role of miR-142a-3p in vascular development and integrity," *PLoS ONE*, vol. 7, no. 12, Article ID e52588, 2012.
- [12] C. E. Gauwerky, K. Huebner, M. Isobe, P. C. Nowell, and C. M. Croce, "Activation of MYC in a masked t(8;17) translocation results in an aggressive B-cell leukemia," *Proceedings of the National Academy of Sciences of the United States of America*, vol. 86, no. 22, pp. 8867–8871, 1989.

- [13] W. Kwanhian, D. Lenza, J. Alles et al., "MicroRNA-142 is mutated in about 20% of diffuse large B-cell lymphoma," *Cancer Medicine*, vol. 1, no. 2, pp. 141–155, 2012.
- [14] M. Lv, X. Zhang, H. Jia et al., "An oncogenic role of miR-142-3p in human T-cell acute lymphoblastic leukemia (T-ALL) by targeting glucocorticoid receptor- α and cAMP/PKA pathways," *Leukemia*, vol. 26, no. 4, pp. 769–777, 2012.
- [15] L. Wu, C. Cai, X. Wang, M. Liu, X. Li, and H. Tang, "MicroRNA-142-3p, a new regulator of RAC1, suppresses the migration and invasion of hepatocellular carcinoma cells," *FEBS Letters*, vol. 585, no. 9, pp. 1322–1330, 2011.
- [16] Y. Lee, M. Kim, J. Han et al., "MicroRNA genes are transcribed by RNA polymerase II," *The EMBO Journal*, vol. 23, no. 20, pp. 4051–4060, 2004.
- [17] W. Yuan, W. Sun, S. Yang et al., "Downregulation of microRNA-142 by proto-oncogene LMO2 and its co-factors," *Leukemia*, vol. 22, no. 5, pp. 1067–1071, 2008.
- [18] Y. Sun, J. Sun, T. Tomomi et al., "PU.1-dependent transcriptional regulation of miR-142 contributes to its hematopoietic cell-specific expression and modulation of IL-6," *Journal of Immunology*, vol. 190, no. 8, pp. 4005–4013, 2013.
- [19] N. Takayama, S. Nishimura, S. Nakamura et al., "Transient activation of c-MYC expression is critical for efficient platelet generation from human induced pluripotent stem cells," *Journal of Experimental Medicine*, vol. 207, no. 13, pp. 2817–2830, 2010.
- [20] Y. Kumaki, M. Oda, and M. Okano, "QUMA: quantification tool for methylation analysis," *Nucleic Acids Research*, vol. 36, pp. W170–W175, 2008.
- [21] P. H. Gunaratne, "Embryonic stem cell MicroRNAs: defining factors in induced pluripotent (iPS) and cancer (CSC) stem cells?" *Current Stem Cell Research & Therapy*, vol. 4, no. 3, pp. 168–177, 2009.
- [22] B. G. Herrmann, S. Labeit, A. Poustka, T. R. King, and H. Lehrach, "Cloning of the *T* gene required in mesoderm formation in the mouse," *Nature*, vol. 343, no. 6259, pp. 617–622, 1990.
- [23] G. Barreto, A. Schäfer, J. Marhold et al., "*Gadd45a* promotes epigenetic gene activation by repair-mediated DNA demethylation," *Nature*, vol. 445, no. 7128, pp. 671–675, 2007.
- [24] G. Escher, A. Hoang, S. Georges et al., "Demethylation using the epigenetic modifier, 5-azacytidine, increases the efficiency of transient transfection of macrophages," *Journal of Lipid Research*, vol. 46, no. 2, pp. 356–365, 2005.
- [25] L. Han, P. D. Witmer, E. Casey, D. Valle, and S. Sukumar, "DNA methylation regulates microRNA expression," *Cancer Biology and Therapy*, vol. 6, no. 8, pp. 1290–1294, 2007.
- [26] M.-R. Suh, Y. Lee, J. Y. Kim et al., "Human embryonic stem cells express a unique set of microRNAs," *Developmental Biology*, vol. 270, no. 2, pp. 488–498, 2004.
- [27] J. Mazar, D. Khaitan, D. DeBlasio et al., "Epigenetic regulation of microRNA genes and the role of miR-34b in cell invasion and motility in human melanoma," *PLoS ONE*, vol. 6, no. 9, Article ID e24922, 2011.
- [28] J. M. Polo, E. Anderssen, R. M. Walsh et al., "A molecular roadmap of reprogramming somatic cells into iPS cells," *Cell*, vol. 151, no. 7, pp. 1617–1632, 2012.
- [29] T. S. Mikkelsen, J. Hanna, X. Zhang et al., "Dissecting direct reprogramming through integrative genomic analysis," *Nature*, vol. 454, no. 7200, pp. 49–55, 2008.
- [30] D. D. de Carvalho, J. S. You, and P. A. Jones, "DNA methylation and cellular reprogramming," *Trends in Cell Biology*, vol. 20, no. 10, pp. 609–617, 2010.
- [31] Y. Wang, J. Gu, J. A. Roth et al., "Pathway-based serum microRNA profiling and survival in patients with advanced stage non-small cell lung cancer," *Cancer Research*, vol. 73, no. 15, pp. 4801–4809, 2013.
- [32] Z. Lei, G. Xu, L. Wang et al., "MiR-142-3p represses TGF- β -induced growth inhibition through repression of TGF β R1 in non-small cell lung cancer," *The FASEB Journal*, vol. 28, no. 6, pp. 2696–2704, 2014.
- [33] T. Watabe and K. Miyazono, "Roles of TGF- β family signaling in stem cell renewal and differentiation," *Cell Research*, vol. 19, no. 1, pp. 103–115, 2009.
- [34] G. Carraro, A. Shrestha, J. Rostkovius et al., "miR-142-3p balances proliferation and differentiation of mesenchymal cells during lung development," *Development*, vol. 141, no. 6, pp. 1272–1281, 2014.

